



**VICTORIA UNIVERSITY**  
MELBOURNE AUSTRALIA

*A review of experimental and numerical studies of lithium ion battery fires*

This is the Published version of the following publication

Ghiji, Mohammadmahdi, Edmonds, Shane and Moinuddin, Khalid (2021) A review of experimental and numerical studies of lithium ion battery fires. *Applied Sciences (Switzerland)*, 11 (3). pp. 1-29. ISSN 2076-3417



The publisher's official version can be found at  
<https://www.mdpi.com/2076-3417/11/3/1247>

Note that access to this version may require subscription.

Downloaded from VU Research Repository <https://vuir.vu.edu.au/42857/>

Review

# A Review of Experimental and Numerical Studies of Lithium Ion Battery Fires

Matt Ghiji , Shane Edmonds and Khalid Moinuddin 

Institute of Sustainable Industries and Liveable Cities, Victoria University, Melbourne, VC 8001, Australia; sedmonds@affinity-eng.com (S.E.); khalid.moinuddin@vu.edu.au (K.M.)

\* Correspondence: Mohammadmahdi.Ghiji@vu.edu.au; Tel.: +61-3-9919-8084

**Abstract:** Lithium-ion batteries (LIBs) are used extensively worldwide in a varied range of applications. However, LIBs present a considerable fire risk due to their flammable and frequently unstable components. This paper reviews experimental and numerical studies to understand parametric factors that have the greatest influence on the fire risks associated with LIBs. The LIB chemistry and the state of charge (SOC) are shown to have the greatest influence on the likelihood of a LIB transitioning into thermal runaway (TR) and releasing heats which can be cascaded to cause TR in adjacent cells. The magnitude of the heat release rate (HRR) is quantified to be used as a numerical model input parameter (source term). LIB chemistry, the SOC, and incident heat flux are proven to influence the magnitude of the HRR in all studies reviewed. Therefore, it may be conjectured that the most critical variables in addressing the overall fire safety and mitigating the probability of TR of LIBs are the chemistry and the SOC. The review of numerical modeling shows that it is quite challenging to reproduce experimental results with numerical simulations. Appropriate boundary conditions and fire properties as input parameters are required to model the onset of TR and heat transfer from thereon.



**Citation:** Ghiji, M.; Edmonds, S.; Moinuddin, K. A Review of Experimental and Numerical Studies of Lithium Ion Battery Fires. *Appl. Sci.* **2021**, *11*, 1247. <https://doi.org/10.3390/app11031247>

Academic Editor:  
Cheol-Hong Hwang  
Received: 1 January 2021  
Accepted: 26 January 2021  
Published: 29 January 2021

**Publisher's Note:** MDPI stays neutral with regard to jurisdictional claims in published maps and institutional affiliations.



**Copyright:** © 2021 by the authors. Licensee MDPI, Basel, Switzerland. This article is an open access article distributed under the terms and conditions of the Creative Commons Attribution (CC BY) license (<https://creativecommons.org/licenses/by/4.0/>).

**Keywords:** lithium-ion battery; thermal runaway; heat release rate; state of charge; fire; incident heat flux

## 1. Introduction

The world is currently changing environmentally in a negative direction due to the greenhouse effect that poses a direct threat to humanity. The main contributor to these unfavorable changes is CO<sub>2</sub> emissions from the combustion of fossil fuels accounting for 87% of the human-produced CO<sub>2</sub> emissions [1]. The main contributor is the electricity/heat and transportation industry, which contributes nearly two-thirds of the total CO<sub>2</sub> emissions globally [2]. To reduce future CO<sub>2</sub> emissions, greater emphasis has been placed on ecofriendly energy sources such as solar and wind energy systems. Storage systems are required to supply secure and reliable electricity 24 h a day; lithium-ion batteries (LIBs) are currently at the forefront of energy storage technologies.

Lithium-ion batteries offer high energy and power density, are lightweight, and have a long lifespan. LIBs are used in an extensive range of applications which can be categorized into the three main industries—consumer electronics, automotive, and grid storage. Therefore, there is an intense interest in the research and initiatives in this field from both industry and government funding agencies. Fire is a major safety concern with the ever-increasing demand for energy storage devices worldwide. The incidence of reported LIB fires is somewhere in the vicinity of one in one million and one in 10 million units [3]. While the probability of a LIB fire on face value does not fit within the realms of a high-risk item, the hazard arises from the sheer volume of lithium batteries being used globally.

In the current climate, the pressure on manufacturers to produce high energy density, high efficiency, long-cycle life batteries with minimal memory effect comes with associated

fire safety risks due to the unique chemical composition properties, higher levels of stored energy, and the flammability of the most electrolytes [4]. In the past five years, there have been a number of fires and explosions involving LIBs which have resulted in both damages to property and injuries to people. When the internal temperature of a LIB increases to approximately 80 °C the solid–electrolyte interphase (SEI) of the battery may decompose and generate more heat [5–7]. If this produced heat does not dissipate, the battery temperature will elevate further, thereby accelerating the process of heat release. This process is known as thermal runaway (TR) and can be triggered by internal or external means. The abuse conditions which may lead to the TR and fire in LIBs can fall into three categories [8]: electrical abuse (overcharging/discharging) [9–14], thermal abuse (overtemperature) [5,15–18], and mechanical abuse [19,20].

Heat release rate (HRR) is considered the most critical parameter when specifying the hazard of fire [21–23], defined as the rate at which the fire releases energy (power). The state of charge (SOC) of LIBs can influence the onset of TR as well as the magnitude of the HRR as the more energy a battery has stored, the more energetic the exothermic reactions of the principal components will be. As more heat and gas are generated in the reactions, the more likely it is that the propagated heat to surrounding cells initiates a fire and explosion, and results in a catastrophic chain reaction [6]. We will, therefore, review past studies on the effect of SOC on TR onset and HRR magnitude.

An integral contributor in the design and virtual prototyping of all things involving fluid (including flame and smoke) is computational fluid dynamics (CFD), which is used in a variety of ways, from complementing experiments to testing and certification of the performance, safety, and reliability of a varied array of systems. CFD has become an important tool in fire safety by helping to determine the expected behavior of fire and smoke in many circumstances where it may be impossible to conduct realistic experiments on complete systems. CFD models allow with the use of quantified experimental data these conditions to be simulated with a commensurate level of accuracy. The most imperative variable in fire simulation is the progression of the HRR with time. In full-scale fire scenarios, the HRR is rarely obtainable, only controlled laboratory experiments under specific conditions provide an accurate measurement of the evolution of the HRR. Such HRR values from laboratory scales can be normalized in terms of per unit surface area (normalized HRR,  $\text{W m}^{-2}$ ) and used as inputs to larger scale CFD simulations. Hence, the tabulation of the HRR data from such experiments is critical in the process of validating/determining other parameters such as time to TR to adjacent battery cells, surrounding air and solid surface temperature, etc., using CFD modeling. Similarly, onset temperature for TR is also an important parameter that needs to be prescribed to the CFD models as modeling the TR process can be very complex.

## 2. Method

This review was conducted to provide an impartial overview of the available research papers including experimental and numerical data of fire testing involving LIBs. Brereton et al. [24] defines such research papers in a review as the primary studies while the review itself forms the secondary study. As the systematic reviews are concerned with the issue of aggregating empirical evidence, several steps need to take place. For any evidence-based approach, aggregation is the essence to offer objective summaries of existing experimental and numerical data. Khan et al. [25] suggested a stepwise process for the systematic review, and this has been adopted here. Our process comprises five steps: framing questions, identifying relevant research studies, assessing the quality of studies, summarizing the evidence, and finally the challenges and future works similar to Tan et al. [26].

In the fire step, we framed the following questions: (1) What are the effects of state of charge on thermal runaway (in terms of temperature and time to ignition) and fire intensity (in terms of HRR)? (2) What numerical modelings of LIB fire have been conducted? (3) What future studies need to be conducted for the safety of LIB? We also considered looking at studies involving LIB chemistry to obtain a better understanding of underlying science.

We identified relevant works in the second step. Journal articles were retrieved from diverse fields of study: fire science, chemical engineering, urban public safety, materials science and engineering, nuclear and new energy technology, mechanical and electronic engineering, and physics. We searched several databases including ScienceDirect, Elsevier, Taylor and Francis, Sage journals, Wiley, Google Scholar, and American Society of Civil Engineers (ASCE) library. In the third step, the quality of the studies was assessed. First, by reading the abstract of the paper, results were identified to reconfirm their applicability. Once reconfirmed, the entire paper was studied. To maintain quality, only peer-reviewed journals, conference proceedings, and books from reputable publishers were considered. In the fourth step, answers to the framed questions were sought and analyzed. In the last step, some suggestions were made for future studies in relation to identified research gaps.

### 3. LIB Chemistry

Li-ions flow from the cathode (positive electrode) to the anode (negative electrode) when charging; during discharge, Li-ions flow from the anode to the cathode. The electrodes are separated by a thin porous membrane (separator), generally polyolefin (PO); electrolyte (typically a combination of lithium salts in an organic solvent) soaks these components and provides the medium for the Li-ions and other molecules to flow [19]. Typically, five components comprise a LIB and are shown in Table 1.

**Table 1.** Typical components of lithium-ion batteries (LIBs) and their compositions [19].

| Component         | Common Composition                                                                                 |
|-------------------|----------------------------------------------------------------------------------------------------|
| Anode             | Graphitic carbons, hard carbons, synthetic graphite, LTO, tin-based alloys, silicon-based alloys   |
| Cathode           | LMO, LCO, NCA, NMC, LFP, ECPs                                                                      |
| Electrolyte       | Lithium salts (mostly LiPF <sub>6</sub> ) in organic solvents such as EC, DEC, DMC, PC, GBL, RTILs |
| Separator         | Polypropylene, polyethylene, cellulosic paper, nonwoven fabrics, ceramic                           |
| Current Collector | Copper for anode<br>Aluminum for cathode                                                           |

LTO: lithium titanate, LMO: lithium manganese oxide, LCO: lithium cobalt oxide, NCA: lithium nickel cobalt aluminum oxide, NMC: lithium nickel manganese cobalt oxide, LFP: lithium iron phosphate, ECPs: electronic conducting polymers, EC: ethylene carbonate, DEC: diethyl carbonate, DMC: dimethyl carbonate, PC: propylene carbonate, GBL: gamma butyrolactone, RTILs: room temperature ionic liquids.

#### 3.1. Cathode and Anode

The two most critical parameters when evaluating the performance of a LIB are the power/energy density and capacity. The energy density of a device is the product of the specific capacity of the material used in the electrodes and the operational voltage from the cathode to the anode [27]. A significant number of studies have been conducted on the structure of the electrode materials. The specific capacity of the common materials used has been fully exploited with most new research exploring the electrochemical potentials of materials to produce batteries with higher voltages, due to the greater difference in lithium chemical potential between the cathode and anode.

LIB materials largely consist of insertion-type or intercalation electrodes, meaning lithium cations (Li<sup>+</sup>) are merged into a host structure and upon charge and discharge the Li<sup>+</sup> is reversibly merged via intrinsic one, two- or three-dimensional openings to facilitate the Li<sup>+</sup> transport without “in theory” any significant change to the host structure. Insertion/intercalation materials are predominantly used due to the high cycling capacity and the minimal variation in volume changes between the discharged and charged states of the cathode and anode. The negative aspect of the insertion/intercalation material is the need for the host structure which is essentially “excess baggage” and thus, reduces the energy density of the cell [28,29]. Alternatively, alloying and conversion mechanisms are also utilized whereby in the case of alloying Li<sup>+</sup> is inserted into the crystal structure of the



electrode (direct bonding with the host structure) in the reactant phase. The conversion mechanism has Li-ions inserted into the nanosized binary compounds resulting in a reduction of cations and the formation of Li anions. The benefits of the alloying and the conversion mechanisms are the high energy density, relatively low cost, environmental compatibility, and the safe operation potentials [30]. The main disadvantages are the short cycle life and the irreversible loss of capacity due to the large volume expansion during the insertion of lithium ions [30]. The repeated expansion and reduction have been shown to cause fracturing of the electrode material, effectively disconnecting portions within the electrode. Additionally, dendrite formation across the cells and through the separator leading to internal short circuit (ISC) caused by electrochemical plating is an on-going concern as the mechanism of dendrite growth is still very much under debate [27,31].

### 3.2. Electrolyte

The electrode materials, particularly the cathode, govern the energy and power density capacities. Electrolyte determines the power density (current), reliability, and safety of the battery (due to the interaction that it has with all other components) and the formation of the SEI. The requirement for the electrolyte to interact with both electrodes necessitates a certain level of chemical stability, thereby limiting the operational scope of the electrolyte material. The SEI whose formation and physical properties depend on the nature of the electrodes (particularly the anode) ensures the chemical compatibility [32].

Typically, the electrolytes used for LIBs are composed of a lithium salt ( $\text{LiPF}_6$  most commonly) within a mixture of flammable organic carbonates. Ethylene carbonate (EC) is combined with dimethyl carbonate (DMC) or diethyl carbonate (DEC). The organic carbonates provide a combination of relatively high chemical stability, low electronic conductivity, low viscosity, and high ionic conductivity. EC is used as the electrolyte solvent in the majority of LIBs; once decomposed it forms a stable SEI on the anode during the first cycle of charging.

Research on the thermal instability of electrolyte has been carried out since the inception of LIBs, and considerable examination into the development of safer electrolytes by providing more stable lithium salts [33,34], which utilize nonflammable solvents [35,36], electrolyte additives [35,36], ionic liquid [37–39], aqueous electrolytes [40,41], polymer electrolytes [42–44], and solid-state electrolytes [45–48]. At present, the most viable solutions in providing a safer electrolyte center around the stability of lithium salts and solvents that are nonflammable [45].

### 3.3. Separator

The separator provides the physical separation between the positive and negative electrodes, which prevents an electrical short circuit between the electrodes. Additionally, the separator acts as the electrolyte reservoir for the transport of Li-ions during the discharge and charging process. Upon failure of the separator, a short circuit between the anode and cathode occurs, which likely leads to thermal failure of the LIB. The following factors are considered critical requirements of the separator: (1) chemical/mechanical stability, (2) thickness, (3) thermal stability, (4) wettability, (5) barrier property, and (6) porous property. Polyolefin-based membranes such as polyethylene (PE), polypropylene (PP), and PP/PE/PP composite membranes have been the most commonly used as separators in LIBs due to their robust mechanical properties, low cost, and chemical stability [49]. Various composite materials including bromine have been investigated as being able to improve the flame retardancy (FR) of the separator while maintaining the critical parameters listed above.

Recently most research efforts have been dedicated to improving the performance of the polyolefin-based separators through the surface coating, coated PO membranes, ceramic blended PE membranes [50–53], ceramic filled nonwovens, and nanofiber separators [54,55], and additives to improve the wettability of the separator towards nonaqueous electrolytes [56].

Li [57] published results from experimental work on the development of plasma-treated polypropylene nonwoven-based composites for high-performance LIB separators. When fluorinated segments are introduced onto the surface of PP nonwoven through plasma treatment, the composite separators display increased electrolyte uptake and ionic conductivity in addition to the electrochemical stability and discharge capacity. Kong [58] presented a study in which they present an in situ formed silica@silica-embedded polyimide (in situ  $\text{SiO}_2@(\text{PI}/\text{SiO}_2)$ ) nanofabric as a new high-performance inorganic—organic hybrid separator.

#### 4. Thermal Runaway

TR is the phenomenon that poses the most significant scientific obstacle regarding LIB safety research, the mechanisms of which are yet to be clearly comprehended [7]. Semenov's plot [59], as shown in Figure 1, graphically depicts the rate of the reaction change as a function of the temperature (exponential function) and the heat removal rate (linear function) at different coolant temperatures.

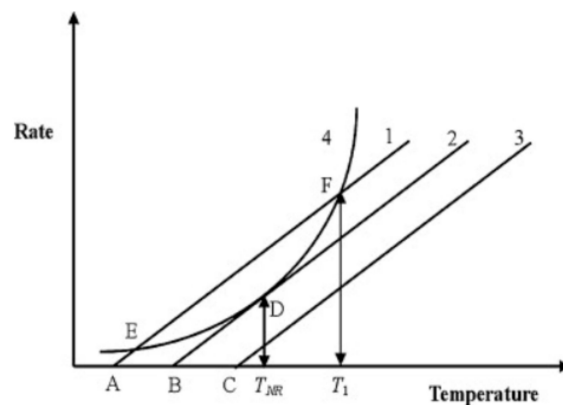


**Figure 1.** Semenov's plot depicting the reaction rate of change as a function of the temperature (exponential function) and the heat removal rate (linear function) at different coolant temperatures [59].

Vessel A is stable at the point E intersection and can absorb a rise until point F ( $T_1$ ) where it reaches instability. Vessel B is unstable and at the point D intersection, the temperature of no return ( $T_{NR}$ ) is reached. When the battery temperature increases to  $T_{NR}$ , the LIB will go to a thermal runaway. Vessel C is stable at no point in time.

To get a clearer insight into the dynamic of TR in LIB, heat sources in LIB during normal operating conditions and elevated temperature should be comprehended. During the normal operating condition, the total heat released in LIB is the sum of reversible heat generated by the electrochemical reactions and irreversible heat produced by the charging/discharging process [60–62]:

$$Q_{\text{tot}} = Q_{\text{rev}} + Q_{\text{rxn}} \quad (1)$$

$$Q_{\text{rev}} = -I \times T \times (\partial E_{\text{oc}} / \partial T) = -a_s \times J \times F \times T \times (\partial E_{\text{oc}} / \partial T) \quad (2)$$

$$Q_{\text{rxn}} = I \times (E_{\text{oc}} - E) = a_s \times J \times F \times (E_{\text{oc}} - E) \quad (3)$$

where  $I$  is the current,  $T$  is the absolute temperature,  $E_{\text{oc}}$  is the open circuit potential,  $E$  is the potential of cell,  $(E_{\text{oc}} - E)$  is the overpotential accounting for irreversibilities such as ohmic losses, charge-transfer overpotential and mass-transfer limitation,  $a_s$  is a specific interfacial area of the electrode,  $J$  is the transfer current that resulted from the intercalation/deintercalation of lithium, and  $F$  is the Faraday constant.

During abnormal operating conditions (abuse conditions), the temperature of LIB may increase and exceed the safe/normal operating condition, which may consequently lead

into TR. The abuse conditions include mechanical abuse, electrical abuse, and environmental abuse [63]. Table 2 shows the abuse conditions and possible causes.

**Table 2.** Abuse conditions and potential causes.

| Abuse Condition | Direct Cause                                                                    |
|-----------------|---------------------------------------------------------------------------------|
| Thermal         | Overheat<br>Extreme cold<br>Fire<br>Thermal shock                               |
| Mechanical      | Shock<br>Drop<br>Penetration<br>Immersion<br>Crush<br>Vibration                 |
| Electrical      | External short circuit<br>Internal short circuit<br>Overcharge<br>Overdischarge |

All three abuse conditions can lead to an ISC (most common pathway to TR), which initiates a sequence of chain reactions [64]. The exothermic reactions required to initiate TR have been documented to begin earlier, but temperatures in excess of 80 °C are typically required to begin the breakdown of the SEI [5–7]. Once this stage is complete and given further increases in temperature, reactions between the anode and electrolyte take place. These initial reactions are followed by larger cathode–electrolyte reactions. Most experimental studies indicate that the point at which the effects of TR cannot be reversed is in the range 150–200 °C [5,64–67]. An overview of the TR process from the abuse conditions leading to the ISC and initiation of TR, exothermic reactions, swelling/venting, and cell case rupturing/explosion/fire is shown in Figure 2. The released heat can propagate to adjacent cells and induce an additional thermal event in the battery pack/module/system. The heat released through each process is discussed and quantified in Section 5.1.

In addition to the thermal abuse conditions that have been widely investigated [7,65–69], the nail penetration [53,70–79] (mechanical abuse) and overcharge [9,10] (electrical abuse) for initiating failure mechanisms are also studied. In the nail penetration tests, the joule heat with a high rate is generated as the steel nail provides an internal current path between the electrodes and current collectors, and electrodes connect to each other due to the deformation. In the overcharge tests, the excessive irreversible lithium removal from the cathode increases the cathode resistance and subsequently raises the LIB temperature due to the joule heating, initiates the exothermic reaction between the electrolyte and oxidized cathode, decomposes the cathode materials, and further increases the LIB temperature, which finally leads to TR.

Various measures are employed to prevent LIB fires categorized into inherent safety that examines the composition and behavior of different materials used in the production of LIBs and safety devices, which are incorporated into the design to release high pressure and heat before the onset of TR [3]. These measures are further discussed in Section 4.3.

#### 4.1. State of Charge and Its Effect on Thermal Runaway

The SOC is the most crucial state function of a battery system and can simply be explained as the remaining available capacity of a battery (in amp hours, Ah), which is expressed as a percentage of the rated capacity. From a thermodynamics point of view, SOC is the amount of potential chemical energy remaining within the battery cells.

The effect of SOC has been studied in almost all research investigating the onset temperature, time to TR, and the energetics associated with thermally induced failure of

LIBs. Stoliarov and his coworkers [80–82] established a novel technique known as the copper slug battery calorimeter (CSBC) to measure the heat generated inside the LIB and combined it with oxygen consumption calorimetry to quantify the heat released in the flaming combustion. The slug heats the specimen to initiate the failure process. They reported that most LIB heat released during TR originated from the electric energy of short circuit, chemical reactions, and combustion, where the amount of combustion heat was more than the sum of the other two parts. These studies [80–82] were extended to determine the timing of the safety venting and TR, and associated temperatures in cylindrical 18650 LIBs containing a carbon anode and three different cathodes: lithium cobalt oxide (LCO), lithium nickel manganese cobalt oxide (NMC), and lithium iron phosphate (LFP) at various states of charge (0, 25, 50, and 100%). The temperature at the time of safety venting and TR data are presented in Table 3.

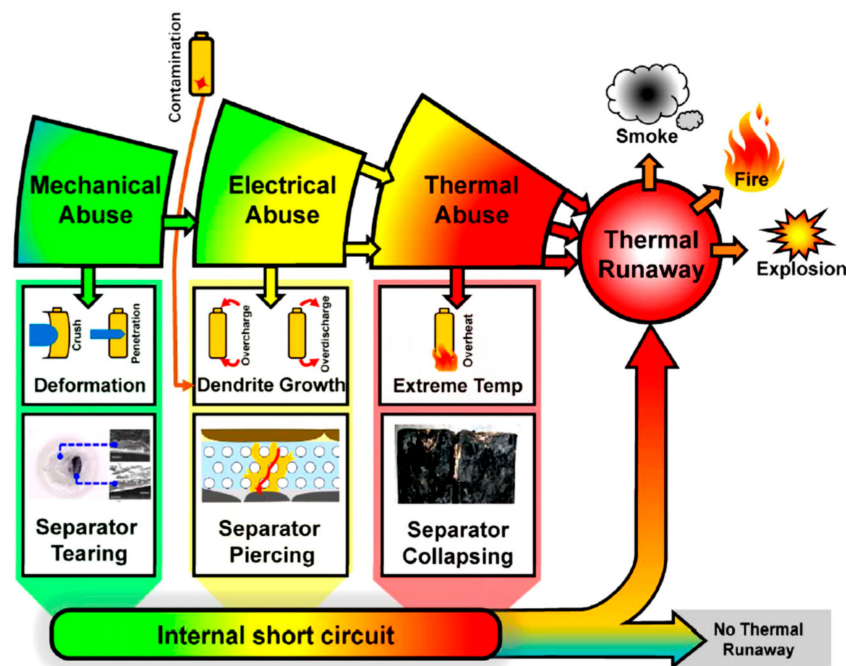


Figure 2. Abuse conditions leading to thermal runaway [7].

Table 3. Temperature of safety venting and thermal runaway [80–82].

| State of Charge | Onset Temperature (°C) |         |         | End Temperature (°C) |          |         |
|-----------------|------------------------|---------|---------|----------------------|----------|---------|
|                 | Safety venting         |         |         |                      |          |         |
|                 | NMC                    | LCO     | LFP     | NMC                  | LCO      | LFP     |
| 0%              | 178 ± 4                | 197 ± 4 | 181 ± 3 | 326 ± 5              | 308 ± 2  | 243 ± 3 |
| 25%             | 177 ± 3                | 195 ± 6 | 198 ± 5 | 238 ± 2              | 232 ± 2  | 240 ± 2 |
| 50%             | 174 ± 4                | 197 ± 4 | 196 ± 6 | 267 ± 3              | 227 ± 2  | 237 ± 2 |
| 100%            | 155 ± 5                | 178 ± 5 | 198 ± 3 | 221 ± 2              | 197 ± 4  | 243 ± 2 |
|                 | Thermal runaway        |         |         |                      |          |         |
|                 | NMC                    | LCO     | LFP     | NMC                  | LCO      | LFP     |
| 0%              | 326 ± 5                | 308 ± 2 | 243 ± 3 | NP                   | NP       | NP      |
| 25%             | 238 ± 2                | 232 ± 2 | 240 ± 2 | 341 ± 2              | 338 ± 5  | 263 ± 3 |
| 50%             | 267 ± 3                | 227 ± 2 | 237 ± 2 | 444 ± 5              | 425 ± 6  | 282 ± 3 |
| 100%            | 221 ± 2                | 197 ± 4 | 243 ± 2 | 454 ± 13             | 428 ± 20 | 311 ± 2 |

Arrows represent upward or downward trend. NP indicates that the data were not provided in the results.

The results in Table 3 indicate that the onset temperatures to TR vary slightly between LIBs used in the research. The LIB at 100% SOC and containing LCO recorded the lowest onset temperature (221 °C) to TR with the onset temperature increasing with decreasing SOC up to 308 °C for the LCO battery at 0%. The NMC battery results were similar with one exception; the LIB at 25% SOC reached the onset of TR 29 °C before the LIB at 50% with a variation of 105 °C between 100 and 0%. The LFP batteries produced a variation of only 6 °C between LIBs at different SOC reaching the onset of TR. The onset temperature to TR is comparable between all LIBs tested and as such there can be no definitive conclusion drawn on the correlation between either SOC or the LIB chemistries to the onset temperature of TR. With the CSBC technique being somewhat new and not widely employed in the testing of LIBs, further studies and data quantification from more industry-accepted methods may be required. The data in relation to the timing of the safety venting for only the LIBs with NMC cathode were measured and are presented in Table 4.

**Table 4.** Timing of safety venting for NMC LIB [80].

| State of Charge | Onset Time (s) | End Time (s) |
|-----------------|----------------|--------------|
| Safety Venting  |                |              |
| 0% ↓            | 1160 ± 27      | 3103 ± 58    |
| 25%             | 1166 ± 36 ↑    | 1685 ± 16    |
| 50%             | 1105 ± 39      | 1697 ± 31    |
| 100% ↓          | 899 ± 39       | 1366 ± 35    |
| Thermal Runaway |                |              |
| 0% ↓            | NP             | NP           |
| 25%             | 1685 ± 16      | 2221 ± 27 ↑  |
| 50%             | 1697 ± 31      | 2019 ± 36    |
| 100% ↓          | 1366 ± 35      | 1556 ± 46    |

Arrows represent upward or downward trend. NP indicates that the data were not provided in the results.

Feng [83] conducted a study into the TR features of a 25 Ah large-format prismatic battery with an NMC cathode using extended volume-accelerating rate calorimetry (EV-ARC). The results of this study showed that the polyethylene (PE) separator began to breakdown at 123.7 °C and melted at 140 °C, though the ceramic coating did not fail until 250 °C, at which point the electrodes short circuited. Of the four experiments completed in this study [83], the onset temperature ranged 85–105 °C and this is the point at which the SEI began decomposition. The internal battery temperature increased exponentially at the onset of TR, calculated to be 259 °C up to 750 °C, at which point the temperature increase slowed before reaching a maximum internal temperature of 853.5 °C.

Zhong [65] completed a study on TR and the fire behavior of an NMC cathode and a natural graphite anode 18650 LIBs at various SOC using a modified cone calorimeter. The purpose of the study was to investigate TR, fire behavior, temperature and voltage variations, gas generation, and the HRR. A radiative heat source was used to heat the batteries and trigger TR. Traditionally, the radiative heat source is located a predetermined distance away from the battery and exposes one side of the battery directly to the heat source and one side indirectly. However, this study utilized a modified cone calorimeter whereby the 18650 battery was inserted into a cylindrical heater with the intention to provide uniform heating across the entire battery. The application of the conventional cone calorimeter method in determining the exact onset temperature to TR is questionable as the internal temperature alters across the battery due to the direct and indirect exposure to the

radiative heat source. The 18650-type batteries used in this study [65] were NMC cathode and a natural graphite anode. The electrolyte was a solution of  $\text{LiPF}_6$  and a mixture of EC, EMC, and DMC. The batteries were equipped with safety vent ports at the positive end of the battery. Tests were conducted under nine test conditions with at least three repetition times, eight of which utilized a 150 W heat source at 0, 25, 50, 70, 75, 80, 90, and 100% SOC. The ninth test condition used a 200 W heat source at 100% SOC. The test results of onset temperature to TR and HRR are shown in Table 5. Considering other studies reviewed [6,66,80,84–88], it can be concluded that there is a direct correlation between the onset temperature to TR, HRR, and the SOC of the LIBs.

**Table 5.** Thermal runaway (TR) and fire behavior of cylindrical 18650 LIBs at varying state of charge (SOC) [65].

| Condition (SOC)<br>(Assumed 150 W Heating Power<br>Unless Otherwise Stated) | Onset Temperature<br>to TR (°C) | Total Heat<br>Release (kW) | HRR <sub>max</sub> (kW) | Normalized HRR <sub>max</sub><br>(kW m <sup>-2</sup> ) |
|-----------------------------------------------------------------------------|---------------------------------|----------------------------|-------------------------|--------------------------------------------------------|
| 0%                                                                          | 278.0 ± 6.0 ↑                   | NP                         | NP                      | NP                                                     |
| 25%                                                                         | 280.0 ± 19.2                    | NP                         | NP                      | NP                                                     |
| 50%                                                                         | 257.6 ± 12.6                    | NP                         | NP                      | NP                                                     |
| 70%                                                                         | NP                              | 30.29 ± 0.14 ↓             | 2.17 ± 0.35 ↓           | 517.9 ± 83.9 ↓                                         |
| 75%                                                                         | 256.7 ± 8.5                     | NP                         | NP                      | NP                                                     |
| 80%                                                                         | NP                              | 35.32 ± 20.94 ↓            | 2.47 ± 1.58 ↓           | 590.1 ± 378.7 ↓                                        |
| 90%                                                                         | NP                              | 47.86 ± 2.29 ↓             | 3.14 ± 0.36 ↓           | 750.8 ± 85.6 ↓                                         |
| 100%                                                                        | 235.6 ± 7.3 ↓                   | 52.60 ± 8.75 ↓             | 3.75 ± 0.86 ↓           | 895.9 ± 205.1 ↓                                        |
| 100%–200 W                                                                  | 249.6 ± 2.5                     | NP                         | NP                      | NP                                                     |

Arrows represent upward or downward trend. Normalized heat release rate (HRR) is the HRR divided by the battery surface area. NP indicates that the data were not provided in the results.

Perea [84] conducted abusive testing on LIBs to determine the influence of SOC on thermal reactions. Four commercially available cylindrical cells based on LFP with rated capacities of 2.68, 3, and 4 Ah, and lithium nickel cobalt aluminum oxide (NCA) cathode materials were investigated. The cells were cycled to three states of charge: 0, 50, and 100% and thermally analyzed using an accelerating rate calorimeter (ARC). As part of the ARC testing, the cylindrical cells were heated to 50 °C and then followed by a 15 min rest period with the intent to stabilize the cell temperature. During this period, the calorimeter measured the self-heating process and if no exothermic reaction took place within the cell greater than the sensitivity threshold of 0.02 °C min<sup>-1</sup>, then the sequence was repeated, this time with an increase of 5 °C. Nail penetration and crush tests were performed on the cylindrical cells at 100% SOC. Onset temperature, maximum temperature, and exothermic time (103–3221 s) for three SOC's of four types of cells are presented in Table 6.

The results show that cells at 100% SOC have the lowest onset to TR temperatures. The onset temperature for NCA (1) is considerably lower than NCA (2) and NCA (3), reported to be due to the difference in the unknown electrolyte used by different manufacturers, which leads to variations in the level of thermal stability of the SEI film. NCA (2), NCA (3), and LFP cells showed only minor or zero temperature variation between onset temperatures for cells at 50 and 100% SOC. NCA (1) cells at 50 and 100% SOC recorded an onset temperature variation of 24.6 °C. No notable onset temperature difference between cells at 0 and 50% SOC was recorded for NCA (1), whilst considerable temperature variations were recorded for all other cells at 0 and 50% SOC. The exothermic reaction time (first exothermic reaction to the completion of TR) was also recorded. The results indicated that the time was shorter for the fully charged cells. The NCA (2) cell had a very short exothermic time of 103 s compared to 996 s for the NCA (1) cell with both at 100% SOC; no indication of why the disparity in the exothermic time between the 18650 cells was provided. The LFP cell at 0% SOC had the greatest exothermic time of 3221 s.



**Table 6.** State of charge and its effect on thermal runaway characteristics revealed using nail penetration and crush tests [84].

| LIB Chemistry and Format | Rated Capacity (Ah) | SOC (%) | Onset Temperature (°C) | Maximum Temperature (°C) | Exothermic Time (s) |
|--------------------------|---------------------|---------|------------------------|--------------------------|---------------------|
| NCA (1)–18650            | 3.00                | 100     | 51                     | 838                      | 996                 |
|                          |                     | 50      | 75.6                   | 704                      | 1028                |
|                          |                     | 0       | 75.5                   | 320                      | 2093                |
| NCA (2)–18650            | 2.68                | 100     | 100                    | 704                      | 103                 |
|                          |                     | 50      | 100                    | 739                      | 1311                |
|                          |                     | 0       | 120.7                  | 350                      | 1810                |
| NCA (3)–20700            | 2.68                | 100     | 70                     | 679                      | 1297                |
|                          |                     | 50      | 70.5                   | 794                      | 1508                |
|                          |                     | 0       | 125.3                  | 350                      | 1629                |
| LFP–3Ah 26650            | 4.00                | 100     | 100.2                  | 455                      | 1926                |
|                          |                     | 50      | 106                    | 349                      | 2859                |
|                          |                     | 0       | 115                    | 349                      | 3221                |

SOC was also shown to affect the degradation of LFP/graphite batteries in accelerated storage testing completed by Zheng [89]. The study showed that batteries at 100% SOC and at elevated temperatures (55 °C) experienced the greatest levels of capacity fade. This decay of the battery capacity is due in part to the decomposition of the electrolyte at higher temperatures and the side reactions involving the graphite anode at a higher SOC. The findings [89] show that the peak HRR for higher SOC were recorded to be marginally lower than for some of the LIBs at lower SOC, particularly when exposed to higher levels of heat flux. It was hypothesized that this may be attributed to three possible factors:

- Batteries at higher SOC have larger amounts of stored energy leading to more explosive and faster reactions thereby limiting the amount of oxygen consumption, and subsequently incomplete combustion of the LIB;
- Onset of TR occurs earlier for batteries at a higher SOC, resulting in insufficient time to allow chemical reactions to release thermal energy;
- The oxygen (or part of) that is released from the internal electrochemical reactions is consumed in the combustion process, leading to HRR prediction errors based on the oxygen consumption method.

A method to assess the thermal hazard was investigated whereby a ratio of the peak HRR and the time to ignition (TTI) is evaluated. The time to ignition has been defined as the duration of time between sample exposure to the incident heat flux and a visible continuous flame. The results of this as documented in the study indicate that the fire risk increases substantially when either the SOC or the incident heat flux is increased. To further quantify the risks associated with LIB fires, it was proposed to undertake further experimental and theoretical work in the production and emission of toxic gases and explosions.

#### 4.2. Thermal Runaway in Multiple Cells

Lithium-ion cells are available in button, cylindrical, pouch and prismatic shapes. In order to deliver the required power and energy from a battery system, the cells are configured in parallel and/or series to increase the capacity and/or the voltage, respectively. A battery system usually consists of a number of battery packs, which are made of multiple battery modules, each containing a number of cells with series and/or parallel configuration.

For a battery system, in addition to the thermal hazards that are typically observed in a single battery including high-temperature, safety valve burst, venting, combustion, explosion, and toxic gases during TR, the heat propagation to surrounding batteries can be

also exhibited. Within a battery pack, the propagation is a serious thermal hazard which may result into catastrophic consequences; thus countermeasures should be taken into account to cease the failure propagation [10,63,69,90–98].

In a study conducted by Ouyang et al. [69], the fire behaviors of cylindrical 18650 batteries and battery packs under discharge conditions were investigated. Four battery packs (NMC cathode and graphite anode) were used: a single cell, two cells, three cells, and four cells, all of which were positioned and connected electrically in parallel. In total, eight tests were conducted at 100% SOC, four with the discharging treatment and four without. The experiments were performed in a cone chamber with a 2 kW electric heater as the heat source. It was reported that the burning process of the LIBs exhibited four distinct stages: the heating stage, the cracking of the safety vent, battery ignition, and TR. The data of time and temperature to ignition and TR are presented in Table 7. The results indicate that the LIBs under discharge have earlier ignition, earlier ejection of material, and earlier stable combustion than the LIBs not subjected to discharge, and the ejection and combustion is noticeably more intense than the latter. Furthermore, it was found that with increased cell numbers these fire behaviors were amplified. However, temperature to TR did not change significantly.

**Table 7.** The fire behaviors of cylindrical 18650 LIBs (NMC cathode and graphite anode) under discharge conditions [69].

| Test no. | Number of Cells | With Discharging | Time to Ignition (s) | Temperature to Ignition (°C) | Time to TR (s) | Temperature to TR (°C) |
|----------|-----------------|------------------|----------------------|------------------------------|----------------|------------------------|
| 1        | 1               | Yes              | 251                  | 180                          | 295            | 248                    |
| 2        | 2               | Yes              | 225                  | 170                          | 264            | 247                    |
| 3        | 3               | Yes              | 219                  | 172                          | 248            | 247                    |
| 4        | 4               | Yes              | 217                  | 176                          | 242            | 246                    |
| 5        | 1               | No               | 255                  | 180                          | 306            | 248                    |
| 6        | 2               | No               | 234                  | 176                          | 294            | 239                    |
| 7        | 3               | No               | 233                  | 178                          | 283            | 244                    |
| 8        | 4               | No               | 233                  | 175                          | 274            | 242                    |

Ouyang et al. [90] also conducted a comprehensive set of TR propagation tests in cylindrical 18650 packs with different sizes,  $2 \times 2$ ,  $3 \times 3$ , and  $4 \times 4$ . It was reported that the TR, initially induced by external heating of a corner battery, propagated with a domino effect within the entire battery pack. The effects of other parameters such as SOC, first TR location, spacing, and the number of heaters on TR propagation were also investigated. They demonstrated that the failure propagation worsened (earlier TR, faster TR propagation, greater mass loss, and the higher peak temperature) at higher SOC, occurred earlier for the pack with a larger number of heaters, and exacerbated when the TR took place closer to the center of the pack.

Ouyang et al. [91] extended the TR propagation studies by investigating the effects of various battery pack shapes, triangular, rectangular, parallelogramular, linear, hexagonal, and square. The triangle and line packs showed a smaller TR propagation speed compared to the other pack designs. Taking the space utilization also into account, they concluded that the triangular arrangement is the safest design.

The effects of two battery designs, cylindrical and pouch, used in battery packs were tested by Lamb et al. [99], and it was shown that the pouch batteries are more prone to TR propagation compared to the cylindrical batteries due to their maximal contact to the surrounding batteries.

Another parameter that can significantly influence the TR propagation in a battery pack is the tab configuration [92] due to the heat transfer from the tab. Lopez et al. [92] reported that the branched style of tabbing (M-type) enhanced the voltage retention and

subsequently improved the safety of the pack compared to the serpentine style of tabbing (S-type), as shown in Figure 3.

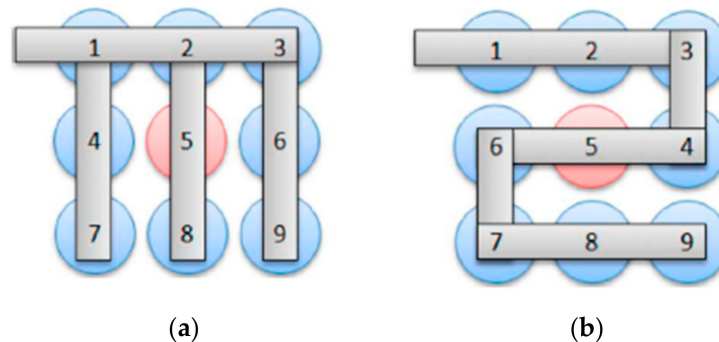


**Figure 3.** Tab configurations of a battery pack: (a) branched style of tabbing (M-type) and (b) serpentine style of tabbing (S-type) [92].

#### 4.3. Mitigating the Risk of Thermal Runaway and Fire

To mitigate the risk and the subsequent consequences associated with TR, researchers have invested considerable time into the modification of the LIB materials. The majority of these studies aimed to improve the inherent safety and decrease the possibility of the hazard by utilizing safety devices and active fire suppression systems to constrain the deterioration of the TR and mitigate fire impacts.

##### 4.3.1. Inherent Safety

The mixture of organic carbonates and lithium salts commonly used in LIBs means that the electrolyte is highly flammable and cause for major safety concerns. FR electrolyte additives mixed with the solvents or completely replacing the flammable solvents is seen as the ideal way to mitigate the risk of an unwanted fire scenario. For an additive to be a viable option, the following characteristics are critical:

1. Good chemical stability, no chemical reaction with battery components;
2. Electrochemical inertia, no adverse electrochemical reactions within the normal operating voltage range of the LIB;
3. Suitable physical properties including conductivity, viscosity, boiling point, density, solubility, etc.;
4. Low toxicity, good machinability, and appropriate cost.

Currently, the most common FR electrolyte additives and alternatives include:

- Phosphorus additives [100–103];
- Fluoride additives [104,105];
- Brominated compound additives [106];
- Composite additives [107,108];
- Ionic liquid [109–116].

Detailed information of each FR electrolyte and additives can also be found in Ouyang et al.'s [64] review paper.

Another component of LIB that has a critical role in securing battery safety is the separator [55,117–119]. There are a number of critical properties associated with separator technology that must be accomplished simultaneously in order to improve the safety and efficiency of LIBs:

- Fire resistance;
- Mechanical properties;
- Thermomechanical stability;
- Ion-transport resistance.

In situ  $\text{SiO}_2@(\text{PI}/\text{SiO}_2)$  was reported to be fire-resistant/nonflammable [58] as it would not ignite when exposed to a fire source. The mechanical properties are considered paramount in device safety. Nonwoven fabric separators are renowned for their weak mechanical properties due to the loose interactions between the different fibers. The in situ  $\text{SiO}_2@(\text{PI}/\text{SiO}_2)$  hybrid separator results [58] show a tensile strength increase at least five times greater than nanofabric devoid of the silica. Furthermore, the storage modulus (maintain structural integrity under compression) was increased at least five times [58].

Thermomechanical stability (the ability to maintain mechanical properties under thermal stress) is a critical parameter for high-power and high-energy-density LIB applications. Providing a thermally and mechanically stable separator improves battery safety significantly when undergoing TR. It was reported that the in situ  $\text{SiO}_2@(\text{PI}/\text{SiO}_2)$  hybrid separator remains thermomechanically stable up to 371 °C [58], which is significantly higher than fabric-based separators. The electrochemical performance of LFP half-cell batteries assembled with the in situ  $\text{SiO}_2@(\text{PI}/\text{SiO}_2)$  hybrid separator showed high capacity and excellent cycling stability with no decay of the battery capacity over 100 cycles at a high temperature of 120 °C [58].

Li [57] published results from experimental work on the development of plasma-treated polypropylene nonwoven-based composites for high-performance LIB separators. When fluorinated segments are introduced onto the surface of PP nonwoven through plasma treatment, the composite separators display increased electrolyte uptake and ionic conductivity in addition to the electrochemical stability and discharge capacity. Kong [58] presented an in situ formed silica@silica-embedded polyimide (in situ  $\text{SiO}_2@(\text{PI}/\text{SiO}_2)$ ) nanofabric as a new high-performance inorganic–organic hybrid separator.

Various synthesized flame retardant composites, including  $\text{Al}_2\text{O}_3$ -sputtered PE separator,  $\text{Al}(\text{OH})_2$ -composite, and  $\text{Mg}(\text{OH})_3$ -composite, showed better flame retardancy compared to the conventional separators [120]. Other separator materials and designs with improved thermal and mechanical properties include polyester fiber nonwoven membranes [55], silica/polyvinylidene fluoride porous composite matrix [121], porous-layer-coated polyimide nanofiber [54], and polyformaldehyde/cellulose nanofiber blends [122].

#### 4.3.2. Safety Devices

Safety devices built into the structure of the battery to mitigate the risk associated with either overcurrent, overtemperature, or pressure are known as current interrupt devices (CID) and positive temperature coefficient (PTC) devices.

The safety or pressure vent is crucial in protecting users from the risk of increased internal pressure of a LIB. The safety vent, composed of a gasket containing a puncture film and a spike, allows the venting of built-up pressure, which inhibits the dangerous rupturing of the battery. The severity or impact of TR is, in part, related to the build-up and subsequent release of pressure from within the cell. When the internal pressure of the LIB reaches a critical limit, the safety vent is designed to rupture and effectively reduces outward pressure on the casing of the cell [4,123–125].

The CID is activated by elevated temperatures commonly caused by overheating, overcharging and short circuiting, functioning when the vapor pressure build up breaks the solder joints welded to the aluminum sheet, releasing the pressure relief sheet that turns over and creates an open circuit with the battery [4].

The main aim of PTC electrodes is to protect LIBs during abnormal electrical conditions such as overcharging and overdischarging, etc. PTC electrodes simply increase their internal resistance drastically with increasing temperature, effectively providing a self-current-limiting capability to reduce the heat generated by LIB reactions [126–131].

#### 4.3.3. Battery Management System

LIBs are required to operate in a variety of conditions such as high and low temperatures. As past research has suggested, temperature impacts the performance of LIBs considerably. The battery management system (BMS) monitors battery parameters and

provides warnings and initiates shutdowns in a system when hazardous conditions are imminent. Therefore, effective BMS that allow regulation of the battery temperature is critical in reducing the occurrence of thermal hazards. BMS are traditionally categorized as internal thermal management (ITM) and external thermal management (ETM). These two categories can be broken down further into the following subcategories:

- Internal management system (IMS)—direct current (DC)→ alternating current (AC) method and component optimization;
- External management system (EMS)—air cooling system (ACS), liquid cooling system (LCS), and phase-change material-based cooling system (PCM-CS).

Early warning provisions for single batteries, such as real-time monitoring of voltage, current, resistance, and other data are expected to be able to provide an indication and subsequent alarm when an abnormal result within the aforementioned variables appears. For battery packs, management monitoring observes and analyses changes in voltage, current, resistance, and other electrical parameters that occur during normal operation of the battery pack—temperature variations and gases that may be escaping. Particular attention focuses on monitoring escaping gas due to the flammable nature of the organic materials; research suggests that sensors used to detect these gases may be able to provide sufficient warning to mitigate the risk of a thermal event [64]. A comparison of EMS is presented in Table 8.

**Table 8.** Comparison of different types of external battery management systems (BMS) [64]. ACS is air cooling system, LCS is liquid cooling system, and PCM-CS is phase-change material-based cooling system.

| BMS    |                                  | Advantages                                                                           | Disadvantages                                                                                    |
|--------|----------------------------------|--------------------------------------------------------------------------------------|--------------------------------------------------------------------------------------------------|
| ACS    | Natural convection               | Low cost; simple structure; easy to integrate; little electricity consumption        | Low heat transfer coefficient; dependent on ambient temperature; uneven temperature distribution |
|        | Forced convection                | Low cost; easy to maintain                                                           | Low efficiency; dependent on ambient environment; insufficient for extreme conditions            |
| LCS    | Liquid cooling                   | Low cost; easy to maintain                                                           | Risk of leakage                                                                                  |
|        | Vapor cooling                    | Higher efficiency; low operating cost; better uniformity                             | Higher cost for structure design; high cost for circulation                                      |
| PCM-CS | Organic<br>Inorganic<br>Eutectic | High efficiency; uniform temperature distribution; appropriate to extreme conditions | Risk of leakage; volume difference with phase change; risk of supercooling                       |

#### 4.3.4. Active Fire Protection Systems

Firefighting of LIB fires comprises the suppression of the open flame fire and attempting to reduce the battery temperature sufficiently to reduce the likelihood of reignition of the battery. Results of experimental studies conducted by the Fire Protection Research Foundation (FPRF) [132], Federal Aviation Administration (FAA) [133], and Det Norske Veritas and Germanischer Lloyd (DNVGL) [134] suggest that water-based extinguishing agents were the most effective to combat LIB fires. For detailed information of LIBs' extinguishing agents, fire protection, and suppression systems, please refer to Ghiji et al.'s review paper [63].

## 5. Heat Release Rate

The HRR is the most critical parameter to define a fire. The HRR can be incorporated (as a source term) into a variety of tools to assess fire and its potential severity. A quantifiable HRR to utilize as an input parameter (source term) for empirical equations, zone modeling, and numerical modeling can lead to the determination of most other quantifiable parameters/variables associated with fire. CFD fire models (such as Fire Dynamics



Simulator, FDS) can specify the fire in terms of HRRPUA (HRR per unit area) and therefore normalized HRR (per unit surface area) are determined and presented here.

### 5.1. HRR Measurement Methodologies

Different methodologies exist to evaluate the HRR with many techniques focused on the mass balance when the heat of combustion of the fuel is known. One main contributor to the heat released during TR, in addition to the heat released by exothermic reactions between battery materials, is the organic electrolyte solvent [135]. The thermochemical and physical properties of the common solvents are shown in Table 9. In this table,  $\Delta H_c$  is the heat of combustion,  $\Delta H_{vap}$  is the heat of vaporization, and  $\Delta_f G^0$  is the standard Gibbs free energy of formation. Usually, the mass fraction of electrolyte is approximately 10% of the cell mass [88,135]. It was reported that maximum effective heat of combustion for a 2.9 Ah (11 Wh) commercial pouch-type lithium manganese oxide (LMO) cell was  $4.03 \pm 0.34 \text{ MJ kg}^{-1}$ , and the electrolyte contribution, calculated using the mass balance, was up to  $1.92 \text{ MJ kg}^{-1}$  [135].

**Table 9.** Thermochemical and physical properties of the commercially available solvents [136,137].

| Solvent   | Molecular Formula                             | Flash point (°C) | Boiling Point (°C) | $\Delta H_c$ (MJ kg <sup>-1</sup> ) | $\Delta H_{vap}$ (MJ kg <sup>-1</sup> ) | $\Delta_f G^0$ (kJ mol <sup>-1</sup> ) |
|-----------|-----------------------------------------------|------------------|--------------------|-------------------------------------|-----------------------------------------|----------------------------------------|
| EC [136]  | C <sub>3</sub> H <sub>4</sub> O <sub>3</sub>  | 146              | 248                | 12.66                               | 0.62                                    | −276.19                                |
| DMC [136] | C <sub>3</sub> H <sub>6</sub> O <sub>3</sub>  | 18               | 91                 | 14.48                               | 0.43                                    | −364.54                                |
| EMC [136] | C <sub>4</sub> H <sub>8</sub> O <sub>3</sub>  | 23               | 110                | 18.41                               | 0.34                                    | −356.12                                |
| DEC [137] | C <sub>5</sub> H <sub>10</sub> O <sub>3</sub> | 445              | 126                | 21.63                               | 0.34                                    | −347.70                                |
| PC [137]  | C <sub>4</sub> H <sub>6</sub> O <sub>3</sub>  | 455              | 242                | 16.56                               | 0.55                                    | −275.48                                |
| EA [137]  | C <sub>4</sub> H <sub>8</sub> O <sub>2</sub>  | 427              | 77                 | 23.77                               | 0.35                                    | −251.12                                |

EC is ethylene carbonate, DMC is dimethyl carbonate, DEC is diethyl carbonate, PC is propylene carbonate, EA is ethyl acetate,  $\Delta H_c$  is the heat of combustion,  $\Delta H_{vap}$  is the heat of vaporization, and  $\Delta_f G^0$  is the standard Gibbs free energy of formation.

In a scenario where there are different burning materials, then calorimetric principles can be utilized. These methods measure and rely on the consumption of oxygen or alternatively the generation of carbon monoxide or carbon dioxide. The most widely used method is the species-based calorimetry or oxygen depletion as it is based on the oxygen mass balance and does not require knowledge of the material chemical composition or combustion chemistry [138]. Often alongside HRR, the TTI is also measured with a cone calorimeter. Single burning item (SBI) and an ISO 9705 room equipped with a calorimeter hood are the other test apparatus used.

### 5.2. HRR and TTI Measured Data for 18650 Batteries

Fu [6] studied the burning behaviors of commercial 18650 2.6 Ah LIBs, (Sanyo-UR18650FM). The cathode material used was LCO with a graphite anode and electrolyte consisting of organic solvents and inorganic salts. Five tests were conducted at various SOC (0, 50, 60, 70, and 100%) exposing the LIBs to an incident heat flux of  $50 \text{ kW m}^{-2}$  using a cone calorimeter in accordance with the ISO 5660-1 with an additional two tests exposing the LIBs at 100% SOC heat fluxes of 30 and  $60 \text{ kW m}^{-2}$ . The results are presented in Table 10. The normalized HRR data are derived from the HRR data by dividing by the battery surface area. The results at  $50 \text{ kW m}^{-2}$  indicate that SOC and the time to peak HRR and the magnitude of the peak HRR for the batteries at 100, 70, and 65% show a similar relationship. The batteries at 0 and 50% SOC, however, show no disposition to this relationship in terms of either time to peak HRR or peak HRR value. LIBs exposed to increased heat flux were shown to reach peak HRR faster and have a peak HRR of greater magnitude; the peak HRR (9.1 kW) of the LIB, when exposed to  $60 \text{ kW m}^{-2}$ , was considerably greater than the peak HRR of the LIBs when exposed to heat fluxes of 50 and  $30 \text{ kW m}^{-2}$  (6.8 and 6.2 kW, respectively). The experimental results indicate that the peak HRR increase as a function of incident heat flux as the chemical reactions between



LIB materials are of greater intensity. This trend was also reported by Huang et al. [139] and thought to be due to the blowing off the fire by the high-speed gas ejection during the TR [139], incomplete combustion of gases as the sudden explosion limits the oxygen consumption [6], and the internally released oxygen involved in the combustion in the relatively short burning process [6].

**Table 10.** HRR versus SOC for 18650 LCO LIBs [6].

| Condition             |                            | Total Energy Released (kJ) | HRR <sub>max</sub> (kW) | Normalized HRR <sub>max</sub> (kW m <sup>-2</sup> ) |
|-----------------------|----------------------------|----------------------------|-------------------------|-----------------------------------------------------|
| SOC                   | 0%—50 kW m <sup>-2</sup>   | 109                        | 1.1                     | 262.9                                               |
|                       | 50%—50 kW m <sup>-2</sup>  | 120                        | 1.5                     | 358.5                                               |
|                       | 65%—50 kW m <sup>-2</sup>  | 104                        | 5.8                     | 1386.2                                              |
|                       | 70%—50 kW m <sup>-2</sup>  | 101                        | 6.5                     | 1553.5                                              |
|                       | 100%—50 kW m <sup>-2</sup> | 100                        | 6.8                     | 1625.2                                              |
| Radiative heat source | 100%—30 kW m <sup>-2</sup> | NP                         | 6.2                     | 1441.8                                              |
|                       | 100%—60 kW m <sup>-2</sup> | NP                         | 9.1                     | 2174.9                                              |

Normalized HRR is the HRR divided by the battery surface area. NP indicates that the data were not provided in the results.

Wang [85] reported on the fire behavior of LIBs at varying states of charge induced by high incident heat fluxes. Bench-scale testing using a cone calorimeter in accordance with the ISO 5660 standard was conducted with the objective to investigate the influence of SOC and external heat flux on the combustion behavior, TTI, and HRR. The fire risk of the LIBs at different SOC and under various heat fluxes was also analyzed. Samsung 18650 LIBs with (NMC) cathode, graphite anode, and an electrolyte consisting of organic solvent and inorganic salt were tested. The LIBs were provided with a burst disk as a safety vent to allow venting in abuse conditions. The batteries were exposed to varying heat fluxes of 25, 30, 50, and 75 kW m<sup>-2</sup>, which were deemed to correspond to a low thermal aggression situation, a mild fire, a flashover situation, and strong and sudden thermal aggression situation. The data are presented in Table 11. When exposed to the same heat flux, the TTI was observed to decrease noticeably with higher SOC. Thornton's principle and Huggett's relation formed the basis for determining the HRR using the oxygen depletion method. The time to peak HRR and the duration of the burning was reported to decrease with increasing SOC, whereas the peak HRR increased with increasing SOC (except for SOC at 0%).

Experimental tests were conducted by Chen [87] using a fire calorimeter to investigate the combustion performance of two separate commercial 18650 LIBs (2.6 Ah Samsung LCO and 1.3 Ah Sony LFP) at various SOC. Five tests were carried out on the Samsung LIB at 0, 25, 50, 75, and 100% SOC while three tests were conducted on the Sony LIBs at 0, 50, and 100% SOC. The maximum heat flux incident on the batteries was 20 ± 0.3 kW m<sup>-2</sup>. The HRR measurement method is based on the oxygen consumption principles in accordance with ISO 9705 and ISO 5660.

The data presented in Table 12 show that LCO with 100% SOC gives 4.1 kW compared to 6.2 kW measured for LCO by Fu [6] at 30 kW m<sup>-2</sup>. The results from testing of the LFP show the magnitude of the maximum HRR peak increases with the increase of the SOC, as observed by Fu [6] and Larsson [86]. However, the result from LCO testing produced was contrary to this, as the LIB at 75% SOC had a greater HRR peak value than the battery at 100% SOC.

**Table 11.** HRR versus SOC for 18650 NMC LIBs [85].

| Condition (SOC) and Radiative Heat Source | Time to Peak HRR (s) | Normalized HRR (kW m <sup>-2</sup> ) |
|-------------------------------------------|----------------------|--------------------------------------|
| 0%—50 kW m <sup>-2</sup>                  | 265.67               | NP                                   |
| 30%—50 kW m <sup>-2</sup>                 | 329.01               | NP                                   |
| 50%—50 kW m <sup>-2</sup>                 | 295.08               | ~710                                 |
| 80%—50 kW m <sup>-2</sup>                 | 265.35               | NP                                   |
| 100%—50 kW m <sup>-2</sup>                | 213.12               | NP                                   |
| 0%—75 kW m <sup>-2</sup>                  | 79.73                | 307.14                               |
| 30%—75 kW m <sup>-2</sup>                 | 110.39               | 589.20                               |
| 50%—75 kW m <sup>-2</sup>                 | 81.34                | 1056.95                              |
| 80%—75 kW m <sup>-2</sup>                 | 86.00                | 814.49                               |
| 100%—75 kW m <sup>-2</sup>                | 78.98                | 848.55                               |
| 50%—25 kW m <sup>-2</sup>                 | NP                   | 557.80                               |
| 50%—35 kW m <sup>-2</sup>                 | NP                   | ~705                                 |
| 50%—50 kW m <sup>-2</sup>                 | 295.08               | ~710                                 |
| 50%—75 kW m <sup>-2</sup>                 | NP                   | 1056.95                              |

Normalized HRR is the HRR divided by the battery surface area. NP indicates that the data were not provided in the results.

**Table 12.** HRR versus SOC for 18650 LCO and LFP LIBs [87] at 20 kW m<sup>-2</sup>.

| Battery Chemistry and SOC (%) | HRR <sub>max</sub> (kW) | Normalized HRR <sub>max</sub> (kW m <sup>-2</sup> ) |
|-------------------------------|-------------------------|-----------------------------------------------------|
| LCO                           |                         |                                                     |
| 0                             | 2.6                     | 621.1                                               |
| 25                            | 4.1                     | 979.9                                               |
| 50                            | 4.9                     | 1171.1                                              |
| 75                            | 5.6                     | 1338.4                                              |
| 100                           | 4.1                     | 979.9                                               |
| LFP                           |                         |                                                     |
| 0                             | 2.0                     | 478.0                                               |
| 50                            | 5.2                     | 1242.8                                              |
| 100                           | 8.3                     | 1983.7                                              |

Normalized HRR is the HRR divided by the battery surface area.

It is observed that sometime higher SOC results in lower HRR, which could be due to blowing off the fire by gas injection during thermal runaway [140].

### 5.3. HRR Data Other than Cone Calorimeter

A series of propane fire tests conducted by Larsson [86] sought to evaluate HRR, toxic species emission, and cell temperature. The LIBs used in the six abuse studies contained a LFP cathode and a carbon-based anode and to give a comparative example, a single test on a laptop battery with a cobalt-based cathode. These tests involved the use of an SBI apparatus used in accordance with the European Classification Scheme EN13823, which is generally used for the classification of building materials. The heat flux was provided by a propane burner placed under the cells and produced approximately 15 kW. The test objects and details are provided in Table 13.

The experimental results for tests 1–5 indicate that the cell at 100% SOC reaches a peak HRR, which far exceeds that of the cells at 50% SOC and 0% SOC. Additionally, the time to the first peak of the cell at 100% SOC is considerably faster than the first and maximum HRR peaks of the cells at 50 and 0%. The results of tests 6 and 7 show that the Lenovo laptop battery pack reaches its peak HRR value faster and has a greater magnitude than the cylindrical K2 cells. It should be noted that the laptop battery packs in this particular test consisted of additional materials, i.e., battery housing and electronic circuits, which may have contributed to these results.

**Table 13.** Evaluation of HRR for different LIBs by a single burning item (SBI) apparatus [86].

| Test no. | Battery Type               | No. of Cells | Nominal Capacity (Ah) | Test Condition        | Time to the Peak HRR (s) | HRR <sub>max</sub> (kW) | HRR <sub>max</sub> (kW)/cell | Normalized HRR <sub>max</sub> (kW m <sup>-2</sup> ) |
|----------|----------------------------|--------------|-----------------------|-----------------------|--------------------------|-------------------------|------------------------------|-----------------------------------------------------|
| 1        | EiG ePLB-F007A             | 5            | 35                    | 100% SOC              |                          | 55                      | 11                           |                                                     |
| 2        | EiG ePLB-F007A             | 5            | 35                    | 100% SOC              | ~90                      | 51                      | 10.2                         |                                                     |
| 3        | EiG ePLB-F007A             | 5            | 35                    | 100% SOC + water mist |                          | 49                      | 9.8                          | 110–490                                             |
| 4        | EiG ePLB-F007A             | 5            | 35                    | 0% SOC                | ~360                     | 13                      | 2.6                          |                                                     |
| 5        | EiG ePLB-F007A             | 5            | 35                    | 50% SOC               | ~200                     | 17                      | 3.4                          |                                                     |
| 6        | K2 LFP26650EV              | 9            | 28.8                  | 100% SOC              | ~390                     | 29                      | 5.8                          | 310                                                 |
| 7        | Lenovo laptop battery pack | 12           | 33.6                  | 100% SOC              | ~200                     | 57                      | 11.4                         | 460                                                 |

Normalized HRR is the HRR divided by the battery surface area.

A full-scale burning test (based on the ISO 9705 full-scale room fire apparatus) of high-energy 50 Ah LFP/graphite battery packs (composed of five identical 10 Ah single cells) was conducted by Ping [88]. The battery dimensions were 91 mm long, 66 mm wide, and 140 mm high, giving a total surface area of 559.72 cm<sup>2</sup>. The results of Ping [88] presented in Table 14 indicate that the LIB at 100% SOC had the largest peak HRR and the battery at 0% had the lowest HRR. The times to the peak HRR are quite comparable, though the higher SOC tends to peak before the LIB at a lower SOC.

**Table 14.** Comparison of HRR and time to peak HRR at varying SOC [88].

| SOC (%)     | HRR <sub>max</sub> (kW) | Time to Peak HRR (s) | Normalized HRR <sub>max</sub> (kW m <sup>-2</sup> ) |
|-------------|-------------------------|----------------------|-----------------------------------------------------|
| 0% peak 1   | 7.7                     | 1629                 |                                                     |
| 0% peak 2   | 12.9                    | 1770                 | 229.6                                               |
| 50% peak 1  | 15.5                    | 1578                 |                                                     |
| 50% peak 2  | 30.1                    | 1655                 | 536.9                                               |
| 50% peak 3  | 20.1                    | 1847                 |                                                     |
| 100% peak 1 | 18.9                    | 1532                 |                                                     |
| 100% peak 2 | 48.4                    | 1705                 | 881.7                                               |
| 100% peak3  | 49.4                    | 1760                 |                                                     |

Normalized HRR is the HRR divided by the battery surface area.

Experimental work on the combustion behavior of LFP/graphite batteries exposed to an external heat source was also conducted by Wang [66]. Electric vehicle 50 Ah batteries were investigated in the ISO 9705 room. The radiant heat source was provided by a 3 kW electric heater. The HRR, among other parameters such as surface temperature, combustion behavior, flame temperature, and mass loss, were recorded. Some data are presented in Table 15. The battery dimensions were 353 mm long, 100 mm wide, and 28 mm high. The batteries were cycled to SOC of 50 and 100%.

**Table 15.** HRR, ignition time, and surface temperature for batteries with 50 and 100% SOC [66].

| Battery Number                       | #1 (50 Ah) | #2 (50 Ah) |
|--------------------------------------|------------|------------|
| SOC %                                | 50         | 100        |
| Peak HRR (kW)                        | 55.93      | 64.32      |
| Normalized HRR (kW m <sup>-2</sup> ) | 587.50     | 675.63     |
| Ignition time (s)                    | 976        | 1108       |
| Surface temperature at ignition (°C) | 124.50     | 128.90     |

It should be noted that the battery at 50% SOC only released a single jet fire and then the combustion became relatively stable with only minor changes to the HRR. For the battery at 100% SOC, no fewer than three jet fire processes were observed. In addition to

the peak HRR, additional peaks of 33.95 and 45.21 kW were recorded at 1895 and 1945 s, respectively.

#### 5.4. Comparative Review of Peak and Normalized HRR

This section presents a comparative analysis of the HRR values obtained at 100% SOC in the reviewed studies. It can be noted that the surface area of 18650 LIB is calculated to be 41.84 cm<sup>2</sup> and is used in all 18650 studies. Batteries of other geometric dimensions show the calculation.

As can be seen from the results shown in Table 16 there is considerable variation in the peak HRR, which is to be expected due to the varying types of LIBs that were used in the studies reviewed. However, the normalized HRR also exhibit a noticeable degree of variation across all LIBs and even across the variety of 18650's. The reason for the variance can be attributed to a number of different factors that may include but not limited to:

- Method of testing;
- Size of external heat sources;
- LIB chemical composition;
- Materials of the LIB, i.e., housing/casing.

**Table 16.** HRR comparisons of LIBs with different electrochemical properties at 100% SOC.

| Battery Type, Study, and Heat Flux Exposure |                                       | Area (cm <sup>2</sup> ) | Peak HRR (KW) | Normalized HRR (kW m <sup>-2</sup> ) |
|---------------------------------------------|---------------------------------------|-------------------------|---------------|--------------------------------------|
| Heat flux exposure                          | LCO 18650 [6]—30 kW m <sup>-2</sup>   | 41.84                   | 6.20          | 1441.80                              |
|                                             | LCO 18650 [6]—50 kW m <sup>-2</sup>   | 41.84                   | 6.80          | 1625.20                              |
|                                             | LCO 18650 [6]—60 kW m <sup>-2</sup>   | 41.84                   | 9.10          | 2174.90                              |
| LFP                                         | Pouch cell [86]—15 kW m <sup>-2</sup> | 80.25                   | 55.00         | 685.60                               |
|                                             | Cylindrical 26650 [86]                | 57.39                   | 29.00         | 1060.80                              |
|                                             | Cylindrical 18650 [87]                | 41.84                   | 8.30          | 1983.70                              |
| Cylindrical 18650                           | LCO [87]                              | 41.84                   | 4.10          | 979.90                               |
|                                             | LFP [87]                              | 41.84                   | 8.30          | 1983.70                              |
| Study                                       | LFP Prismatic cell [88]               | 559.72                  | 49.40         | 881.70                               |
|                                             | LFP Prismatic cell [66]               | 959.2                   | 64.32         | 675.63                               |
| NMC                                         | Cylindrical 18650 [65]                | 41.84                   | 3.75          | 895.90                               |
|                                             | Cylindrical 18650 [85]                | 41.84                   | 3.55          | 848.60                               |

Table 17 provides a comparison between the peak HRR at different SOC for 18650 LIBs reviewed in this paper.

**Table 17.** Peak HRR comparison and the calculated average HRR (kW) for 18650 LIBs at different SOC.

| SOC  | Peak HRR (kW) |          |          |          |          | Average |
|------|---------------|----------|----------|----------|----------|---------|
|      | LCO [6]       | LCO [87] | NMC [65] | NMC [85] | LFP [87] |         |
| 0%   | 1.1           | 2        | NP       | 1.29     | 1.3      | 1.4     |
| 25%  | NP            | 4.1      | NP       | NP       | NP       | NP      |
| 30%  | NP            | NP       | NP       | 2.47     | NP       | NP      |
| 50%  | 1.5           | 4.4      | NP       | 4.42     | 5.1      | 3.9     |
| 65%  | 5.8           | 4.9      | NP       | NP       | NP       | 5.4     |
| 70%  | 6.5           | NP       | 2.17     | NP       | NP       | 4.3     |
| 75%  | NP            | 5.6      | NP       | NP       | NP       | NP      |
| 80%  | NP            | NP       | 2.47     | 3.41     | NP       | 1.94    |
| 90%  | NP            | NP       | 3.14     | NP       | NP       | NP      |
| 100% | 6.8           | 4.1      | 3.75     | 3.55     | 6.8      | 5       |

NP indicates that the data were not provided in the results.

The results from this limited comparison of 18650 cells would suggest that the LFP battery produces the highest HRR at 50 and 100% SOC, and the NMC battery [65] produces the lowest HRR at varying SOC [65]. Based on all studies reviewed within this paper, it may be concluded that LCO and LFP batteries are more reactive and produce a higher HRR than the NMC batteries.

## 6. Modeling of LIBs

Attempts at numerical modeling LIB fire is increasing due to difficulty in conducting experiments. Furthermore, numerical modeling provides a clearer understanding of the chemical-physics associated with the LIBs. Generally, numerical modeling techniques such as CFD and finite element analysis are used to model various stages of fire and or the effect of fire (production of heat and smoke, and their transfer/transport) on surrounding materials. Modeling programs such as FDS, FireFOAM, and ANSYS Fluent allow researchers and manufacturers alike to simulate fire scenarios and estimate parameters such as HRR, heat flux, temperature rise, and smoke production.

Many modeling studies on the TR of LIBs can be found in the literature [10,141–143]. Oven exposure testing of LIBs was replicated using one-dimensional [142] and three-dimensional [143] predictive models. Esho et al. [144] presented an experimental validation method which was able to predict the critical temperature ( $T_{critical}$ ) to TR based on the thermal balance between temperature-dependent heat generation, thermal conduction within the cell, and heat dissipation to the cell surface. A thermal test cell with the geometry of a cylindrical 26650 Li-ion cell was used to determine the value of  $T_{critical}$  in different conditions to compare against the theoretical model. In this study,  $T_{critical}$  was first evaluated theoretically by solving a nonlinear transcendental equation as shown in Equation (4):

$$\frac{Q_0 R^2 E_a}{k \mu^2 R_u T_{critical}^2} e^{\left(-\frac{E_a}{R_u T_{critical}}\right)} - 1 = 0 \quad (4)$$

where  $Q_0$  is the pre-exponential coefficient,  $E_a$  are activation energies,  $R_u$  is the universal gas constant,  $R$  is the cell radius,  $k$  is the cell radial thermal conductivity, and  $\mu$  is the first root of the eigenfunction corresponding to the convective boundary condition at the outer surface of the cell. Using different sets of heat generation and heat dissipation conditions, the theoretical results yielded  $T_{critical}$  temperatures of 35.7 and 44.8 °C. The theoretical results were considered lower than the usually recorded temperatures leading to the onset of TR. The lower  $T_{critical}$  temperatures were selected and utilized in order to safely carry out the experimental works within the thermal test cell. For both  $T_{critical}$  results, the corresponding Arrhenius parameters of combustion or pyrolysis were used as software inputs to ensure that the heat generation followed the corresponding Arrhenius kinetics. The cell temperature was measured as a function of time for different oven temperatures and from this, the oven temperature that results in TR was determined. Esho et al. [144] concluded that when the oven temperature is lower than the theoretically predicted  $T_{critical}$ , the cell temperature remains in a steady state. However, when the oven temperature is in excess of theoretically predicted  $T_{critical}$ , the cell temperatures increase in an uncontrolled fashion, which indicates the onset of TR. Although the temperatures in this study were somewhat below the temperatures associated with and proven to induce TR, the results still provided validation of the theoretical model at low values of  $T_{critical}$ . It is expected that by following the Arrhenius nature of the heat generation, accurate values of larger  $T_{critical}$  can be anticipated.

Anderson et al. [145] completed a study attempting to assess the risk of TR/fire propagating between LIBs. Finite element modeling using the COMSOL multiphysics software that can model conjugate heat transfer to calculate the propagation of heat between adjacent cells was used. The cells were exposed to a 15 kW heat source and the results of the two models (conjugate heat transfer and thermal model) utilized in this study were correlated to experimental data from fire tests where the measured HRR was appropriately used as the input (source term) for the simulations. The commercial Li-ion (EiG ePLB-

F007a 7 Ah) pouch cells had a LFP cathode and a carbon-based anode. Several tests were conducted at different SOC, the experimental data associated with the LIB at 75% SOC were incorporated into the simulations. The complex structure of the pouch cells with the cathode and anode material being layered repeatedly provides difficulties in ascertaining the required thermal property variables such as thermal conductivity, density, and specific heat. In order to obtain reliable and accurate modeling results, precise thermal properties are required. The sheer complexity of the cells makes truly accurate modeling impractical and as such more generalized bulk values of the required thermal properties were used to model the propagative features of the LIBs.

The results of the simulations show deficiencies in both the conjugate heat transfer and thermal models. Uncertain boundary conditions due to the lack of precise details around the test object in a fire scenario lead to less accuracy in the simulation. The boundary conditions are fundamental for computational simulations and inaccurate boundary conditions may lead to the divergence of the results or to the convergence of unrealistic results. Anderson et al. [145] demonstrated that the conjugate heat transfer model and the thermal model correlate well with the experimental data for the first four minutes; however, when the LIB seemingly goes into TR, the results of the modeling deviate from the experimental data significantly. They concluded that this deviation can be attributed in part to the thermal exposure being provided to only the underside of the cells in lieu of around the entire object. Uncertainty over the measured adiabatic surface temperature input values and the fact that the boundaries in a real case are not smooth and sharp, which creates a far more complex convective heat transfer between cells, are thought to contribute to the difference in the real and modelled scenarios.

Feng et al. [146] conducted three-dimensional (3D) TR modeling based on the energy balance equation. The model was built for a large-format prismatic LIB module to investigate TR propagation between adjacent cells. Penetration-induced TR experiments were conducted on large-format LIB modules to validate the 3D TR propagation models. The comparison between the triggering time to TR from one battery to the next for all six cells showed the model to correlate reasonably well with the experimental data. The 3D model also simulated temperature difference at the battery poles between the negative of battery  $i$  and the positive of battery  $i + 1$  at the time when TR was triggered in battery  $i + 1$ . This essentially displays the heat transfer through the battery connector, as shown in Table 18. The values between the experimental and simulation are similar, validating the modeled scenario. As detailed in Table 18, there was only a maximum variation of 25 s in the duration of the TR propagation from cell 4 to cell 5; all others were within 15 s.

**Table 18.** Comparison of the duration of TR propagation from one battery to the next, defined as  $D_{i,i+1}$ , and comparison of the temperature differences through the negative and positive poles of adjacent batteries, defined as  $\Delta T_{p,i,i+1}$  [146].

| Duration (s)     | $D_{1,2}$          | $D_{2,3}$          | $D_{3,4}$          | $D_{4,5}$          | $D_{5,6}$          |
|------------------|--------------------|--------------------|--------------------|--------------------|--------------------|
| Experiment       | 245                | 163                | 186                | 164                | 159                |
| Model            | 236                | 158                | 179                | 189                | 170                |
| Temperature (°C) | $\Delta T_{p,1,2}$ | $\Delta T_{p,2,3}$ | $\Delta T_{p,3,4}$ | $\Delta T_{p,4,5}$ | $\Delta T_{p,5,6}$ |
| Experiment       | 144                | 121                | 183                | 146                | 146                |
| Model            | 141                | 174                | 168                | 165                | 168                |

The four mechanisms or changes proposed to prevent TR propagation within a large format battery module that were modeled clearly show the importance of fire modeling in helping researchers and engineers to better understand and design safer battery modules in regard to TR propagation. The modeling analysis determined the following points:

- The TR triggering temperature is increased by modifying the separator;
- Total electric energy released during TR can be reduced by discharging the battery;
- By increasing the convection coefficient, the heat dissipation can be enhanced;



- TR propagation can be prevented by adding additional thermal layers between adjacent batteries (validated by experiment).

Huang et al. [147] used two classical models to simulate the critical condition of LIB and predict self-accelerating decomposition temperature (SADT) of TR for LIB and TR propagation. The study suggested that there could be potential of TR propagation over neighboring cells when the critical condition based on SADT was reached. There were some discrepancies in actual measured temperatures and predicted SADT temperatures. Between two classical models there also were differences. Huang et al. [147] attributed the difference to the underlying model assumptions and difficulty in measuring temperatures inside the LIBs. To improve further, Huang et al. [148] took the critical parameters of overall reaction as a weighted average of four exothermic reactions and revised the critical criteria by the consumption of reactants. Revised models resulted in an accuracy of within 5 °C when the result of an LCO/graphite cell was compared. Through these revised models, they predicted the critical ambient temperature of the 18650 NCM/LTO battery and analyzed the influences of convective heat transfer coefficient, cell size, and shape to critical condition.

To date, a comprehensive simulation of the fires produced by the flammable gases and other battery materials venting from LIB has not been conducted. Accurate quantification of ejection velocity and temperature of these materials are a challenging subject. So far, most studies aimed to analyze the combustion chemistry of the organic solvents used in LIB [149] or the mixture of the vented gases at TR [150,151].

Johnsplass et al. [151] modelled the laminar burning velocities of the ejecting gases from the LIB premixed with air. It was reported that the burning of vented gases is comparable to propane and methane, presenting a serious hazard of explosion and fires in enclosures, and laminar burning velocities of the gases are similar or slightly higher than that of methane. In another study, Fernandes et al. [150] used a detailed reaction mechanism of flammable gases and DMC to calculate the combustion parameters of the battery venting gases, such as laminar flame velocities, adiabatic flame temperature, and HRR. To date, most of the LIB combustion modeling is limited to the analyses of combustion chemistry in simplified conditions such as premixed or counter flow diffusion flames of the electrolyte carbonated solvents and the venting flammable gases, and simulations of the gas-venting dynamics and their combustion processes are yet to be conducted.

The complex nature of the structure of different LIB cells provides difficulties in ascertaining the required fire property variables such as thermal conductivity, density, specific heat, and Arrhenius parameters. To obtain reliable and accurate modeling results, precise thermal properties are required. Boundary conditions and fire properties are fundamental to computational simulations and inaccurate boundary conditions/fire properties may lead to the unrealistic results which were apparent at the time of and during TR in the study by Anderson et al. [145]. The challenge is determining how a specimen reacts/changes with time in a fire scenario and with so many varied LIB cells comprising of unique chemical compositions, the data required to validate the changing boundary conditions are an ever-evolving commodity. In order to expect realistic simulation results, further experimental studies are required to record and document the fire properties and very fine details of each chemical reaction, particularly around the time of TR initiation within battery cells.

## 7. Conclusions

A review of experimental and numerical studies was conducted, focusing on LIB chemistry, TR, SOC, incident heat flux, HRR, and various numerical modeling methods. The focus of these studies reported in the literature is largely directed toward understanding the parametric effects on TR and HRR. Based on this review, the following conclusions are formulated:

1. The chemical composition of the battery changes both the likelihood of a LIB going into TR and the consequence (energy magnitude of the resultant HRR) for the resultant fire/explosion.

2. The higher SOC leads to shorter time to TR and ignition, and larger magnitude of the rate of energy released (HRR).
3. HRR is considered a major factor after the LIB has gone into TR and the magnitude is directly proportional to the LIB chemistry, the SOC, and incident heat flux.
4. Three-dimensional thermal modeling is challenging. Accurate data for thermal property variables such as thermal conductivity, density, and specific heat are critical to LIB fire modeling. Determining how a test object reacts/changes with time in a fire scenario is critical to the boundary conditions required to complete accurate LIB fire modeling.
5. Three-dimensional thermal modeling has the potential to identify methods to be incorporated in systems to delay or inhibit TR, such as (a) modifying the separator, (b) varying the charging of the battery, (c) changing the convective heat transfer coefficient, and (d) adding additional thermal layers between adjacent batteries.

We compiled HRR data from fire tests of different LIB composition with various SOC. As LIBs tested were of different shapes and sizes, we endeavored to normalize HRR in terms of per unit surface area (HRRPUA). CFD fire models (such as FDS) can specify the fire (as an input or source term) in terms of HRRPUA. We expect that fire modelers will be able to use these data combined with time to TR and TTI data to determine the consequence of LIB fires. However, more future studies need to be conducted to measure HRR magnitude as functions of various parameters so that better HRR function can be developed to use as input to CFD fire models to assess the fire risk. Future studies require more experimental investigations to determine the fire properties of the LIBs and identify very fine details of each chemical reaction, particularly around the time of TR initiation. Additionally, fire tests should involve more instrumentation to record temperatures of surfaces and at the various depths of the packaging, as well as gas temperatures and radiation flux at various distances from the LIBs. These would allow for conducting more faithful numerical simulations and validation. With additional experimental and numerical studies, solutions to prevent or delay TR for reducing fire risk can be found.

It is also observed from this review that different battery testing protocols are used. Furthermore, anecdotal evidence suggests that manufacturers use different standards and protocols, which lead to variations in determining the state of the battery. Therefore, it is recommended that a collaborative effort be undertaken to develop a universal testing standard.

**Author Contributions:** Conceptualization, writing—review and editing, data curation, visualization, and supervision, M.G.; writing—original draft, data curation, and visualization, S.E.; conceptualization, writing—review and editing, data curation, project administration, and supervision, K.M. All authors have read and agreed to the published version of the manuscript.

**Funding:** This research received no external funding.

**Institutional Review Board Statement:** Not applicable.

**Informed Consent Statement:** Not applicable.

**Data Availability Statement:** No new data were created or analyzed in this study. Data sharing is not applicable to this article.

**Conflicts of Interest:** The authors declare no conflict of interest.

## References

1. Shahbazi, A.; Nasab, B.R. Carbon capture and storage (CCS) and its impacts on climate change and global warming. *J. Pet. Environ. Biotechnol.* **2016**, *7*, 4. [[CrossRef](#)]
2. Le Quéré, C.; Peters, G.P.; Andres, R.J.; Andrew, R.M.; Boden, T.A.; Ciais, P.; Friedlingstein, P.; Houghton, R.A.; Marland, G.; Moriarty, R.; et al. Global carbon budget 2013. *Earth Syst. Sci. Data* **2014**, *6*, 235–263. [[CrossRef](#)]
3. Wang, Q.; Ping, P.; Zhao, X.; Chu, G.; Sun, J.; Chen, C. Thermal runaway caused fire and explosion of lithium ion battery. *J. Power Sources* **2012**, *208*, 210–224. [[CrossRef](#)]
4. Balakrishnan, P.G.; Ramesh, R.; Prem Kumar, T. Safety mechanisms in lithium-ion batteries. *J. Power Sources* **2006**, *155*, 401–414. [[CrossRef](#)]
5. Guo, L.S.; Wang, Z.R.; Wang, J.H.; Luo, Q.K.; Liu, J.J. Effects of the environmental temperature and heat dissipation condition on the thermal runaway of lithium ion batteries during the charge-discharge process. *J. Loss Prev. Process Ind.* **2017**, *49*, 953–960. [[CrossRef](#)]
6. Fu, Y.; Lu, S.; Li, K.; Liu, C.; Cheng, X.; Zhang, H. An experimental study on burning behaviors of 18650 lithium ion batteries using a cone calorimeter. *J. Power Sources* **2015**, *273*, 216–222. [[CrossRef](#)]
7. Feng, X.; Ouyang, M.; Liu, X.; Lu, L.; Xia, Y.; He, X. Thermal runaway mechanism of lithium ion battery for electric vehicles: A review. *Energy Storage Mater.* **2018**, *10*, 246–267. [[CrossRef](#)]
8. McDowall, J. A guide to lithium-ion battery safety. *Battcon* **2014**, *1*, 1–23.
9. Ye, J.; Chen, H.; Wang, Q.; Huang, P.; Sun, J.; Lo, S. Thermal behavior and failure mechanism of lithium ion cells during overcharge under adiabatic conditions. *Appl. Energy* **2016**, *182*, 464–474. [[CrossRef](#)]
10. Yuan, Q.; Zhao, F.; Wang, W.; Zhao, Y.; Liang, Z.; Yan, D. Overcharge failure investigation of lithium-ion batteries. *Electrochim. Acta* **2015**, *178*, 682–688. [[CrossRef](#)]
11. Yamamoto, Y.; Kato, K.; Lin, L.; Fukui, M. Athermal management system for lithium-ion battery in mobile systems. In Proceedings of the 2013 European Conference on Circuit Theory and Designs (ECCTD), Dresden, Germany, 8–12 September 2013.
12. McDowall, J. Understanding Lithium-Ion Technology. In Proceedings of the Battcon, Marco Island, FL, USA, 5–7 May 2008.
13. Lisbona, D.; Snee, T. A review of hazards associated with primary lithium and lithium-ion batteries. *Process Saf. Environ. Prot.* **2011**, *89*, 434–442. [[CrossRef](#)]
14. Li, Z.; Huang, J.; Yann Liaw, B.; Metzler, V.; Zhang, J. A review of lithium deposition in lithium-ion and lithium metal secondary batteries. *J. Power Sources* **2014**, *254*, 168–182. [[CrossRef](#)]
15. Lee, C.W.; Venkatachalapathy, R.; Prakash, J. A Novel Flame-Retardant Additive for Lithium Batteries. *Electrochem. Solid-State Lett.* **2000**, *3*, 63–65. [[CrossRef](#)]
16. Joachin, H.; Kaun, T.D.; Zaghbi, K.; Prakash, J. Electrochemical and Thermal studies of LiFePO<sub>4</sub> cathode in lithium-ion cells. *ECS Trans.* **2008**, *6*, 11–16. [[CrossRef](#)]
17. Yang, H.; Bang, H.; Amine, K.; Prakash, J. Investigations of the exothermic reactions of natural graphite anode for Li-ion batteries during thermal runaway. *J. Electrochem. Soc.* **2005**, *152*, A73–A79. [[CrossRef](#)]
18. Spotnitz, R.; Franklin, J. Abuse behavior of high-power, lithium-ion cells. *J. Power Sources* **2003**, *113*, 81–100.
19. Ruiz, V.; Pfrang, A.; Kriston, A.; Omar, N.; Van den Bossche, P.; Boon-Brett, L. A review of international abuse testing standards and regulations for lithium ion batteries in electric and hybrid electric vehicles. *Renew. Sustain. Energy Rev.* **2018**, *81*, 1427–1452. [[CrossRef](#)]
20. Lamb, J.; Orendorff, C.J. Evaluation of mechanical abuse techniques in lithium ion batteries. *J. Power Sources* **2014**, *247*, 189–196. [[CrossRef](#)]
21. Moinuddin, K.A.M.; Thomas, I.R. An experimental study of fire development in deep enclosures and a new HRR-time-position model for a deep enclosure based on ventilation factor. *Fire Mater.* **2009**, *33*, 157–185. [[CrossRef](#)]
22. Moinuddin, K.A.M.; Al-Menhali, J.S.; Prasanna, K.; Thomas, I.R. Rise in structural steel temperatures during ISO 9705 room fires. *Fire Saf. J.* **2011**, *46*, 480–496. [[CrossRef](#)]

23. Vytenis Babrauskas, R.D.P. Heat release rate: The single most important variable in fire hazard. *Fire Saf. J.* **1992**, *18*, 255–272. [[CrossRef](#)]
24. Brereton, P.; Kitchenham, B.A.; Budgen, D.; Turner, M.; Khalil, M. Lessons from applying the systematic literature review process within the software engineering domain. *J. Syst. Softw.* **2007**, *80*, 571–583. [[CrossRef](#)]
25. Khan, K.S.; Ter Riet, G.; Glanville, J.; Sowden, A.J.; Kleijnen, J. *Undertaking Systematic Reviews of Research on Effectiveness: CRD's Guidance for Carrying Out or Commissioning Reviews*; NHS Centre for Reviews and Dissemination: University of York: York, UK, 2001.
26. Tan, S.; Moinuddin, K. Systematic review of human and organizational risks for probabilistic risk analysis in high-rise buildings. *Reliab. Eng. Syst. Saf.* **2019**, *188*, 233–250. [[CrossRef](#)]
27. Liu, C.; Neale, Z.G.; Cao, G. Understanding electrochemical potentials of cathode materials in rechargeable batteries. *Mater. Today* **2016**, *19*, 109–123. [[CrossRef](#)]
28. Pender, J.P.; Jha, G.; Youn, D.H.; Ziegler, J.M.; Andoni, I.; Choi, E.J.; Heller, A.; Dunn, B.S.; Weiss, P.S.; Penner, R.M. Electrode degradation in lithium-ion batteries. *ACS Nano* **2020**, *14*, 1243–1295. [[CrossRef](#)] [[PubMed](#)]
29. Mikolajczak, C.; Kahn, M.; White, K.; Long, R.T. *Lithium-Ion Batteries Hazard and Use Assessment*; Springer Science & Business Media: Berlin/Heidelberg, Germany, 2012.
30. Noel, M.; Suryanarayanan, V. Role of carbon host lattices in Li-ion intercalation/de-intercalation processes. *J. Power Sources* **2002**, *111*, 193–209. [[CrossRef](#)]
31. Yuan, Y.; Amine, K.; Lu, J.; Shahbazian-Yassar, R. Understanding materials challenges for rechargeable ion batteries with in situ transmission electron microscopy. *Nat. Commun.* **2017**, *8*, 15806. [[CrossRef](#)]
32. Li, Q.; Chen, J.; Fan, L.; Kong, X.; Lu, Y. Progress in electrolytes for rechargeable Li-based batteries and beyond. *Green Energy Environ.* **2016**, *1*, 18–42. [[CrossRef](#)]
33. Dahbi, M.; Ghamouss, F.; Tran-Van, F.; Lemordant, D.; Anouti, M. Comparative study of EC/DMC LiTFSI and LiPF<sub>6</sub> electrolytes for electrochemical storage. *J. Power Sources* **2011**, *196*, 9743–9750. [[CrossRef](#)]
34. Li, F.; Gong, Y.; Jia, G.; Wang, Q.; Peng, Z.; Fan, W.; Bai, B. A novel dual-salts of LiTFSI and LiODFB in LiFePO<sub>4</sub>-based batteries for suppressing aluminum corrosion and improving cycling stability. *J. Power Sources* **2015**, *295*, 47–54. [[CrossRef](#)]
35. Feng, J.; Ai, X.; Cao, Y.; Yang, H. Possible use of non-flammable phosphonate ethers as pure electrolyte solvent for lithium batteries. *J. Power Sources* **2008**, *177*, 194–198. [[CrossRef](#)]
36. Feng, J.; Sun, X.; Ai, X.; Cao, Y.; Yang, H. Dimethyl methyl phosphate: A new nonflammable electrolyte solvent for lithium-ion batteries. *J. Power Sources* **2008**, *184*, 570–573. [[CrossRef](#)]
37. Lewandowski, A.; Świdarska-Mocek, A. Ionic liquids as electrolytes for Li-ion batteries—An overview of electrochemical studies. *J. Power Sources* **2009**, *194*, 601–609. [[CrossRef](#)]
38. Francis, C.; Louey, R.; Sammut, K.; Best, A.S. Thermal stability of pyrrolidinium-FSI ionic liquid electrolyte and lithium-ion electrodes at elevated temperatures. *J. Electrochem. Soc.* **2018**, *165*, A1204. [[CrossRef](#)]
39. Moganty, S.; Wu, Y.; Abbate, L.; Brown, K.; Sinicropi, J.; Torres, G. Modified Ionic Liquids Containing Triazine. U.S. Patent Application 16/037,902, 17 January 2019.
40. Takechi, K.; Yang, R. Aqueous Electrolyte with Ethers and Batteries Using the Electrolyte. U.S. Patent 10,193,188, 29 January 2019.
41. Takechi, K.; Yang, R. Aqueous Electrolytes with Protonic Ionic Liquid and Batteries Using the Electrolyte. U.S. Patent Application 15/663,262, 31 January 2019.
42. Zhu, Y.; Wang, X.; Hou, Y.; Gao, X.; Liu, L.; Wu, Y.; Shimizu, M. A new single-ion polymer electrolyte based on polyvinyl alcohol for lithium ion batteries. *Electrochim. Acta* **2013**, *87*, 113–118.
43. Du, Z.; Su, Y.; Qu, Y.; Zhao, L.; Jia, X.; Mo, Y.; Yu, F.; Du, J.; Chen, Y. A mechanically robust, biodegradable and high performance cellulose gel membrane as gel polymer electrolyte of lithium-ion battery. *Electrochim. Acta* **2019**, *299*, 19–26. [[CrossRef](#)]
44. Zhao, L.; Fu, J.; Du, Z.; Jia, X.; Qu, Y.; Yu, F.; Du, J.; Chen, Y. High-strength and flexible cellulose/PEG based gel polymer electrolyte with high performance for lithium ion batteries. *J. Membr. Sci.* **2020**, *593*, 117428. [[CrossRef](#)]
45. Wang, Q.; Jiang, L.; Yu, Y.; Sun, J. Progress of enhancing the safety of lithium ion battery from the electrolyte aspect. *Nano Energy* **2019**, *55*, 93–114.
46. Wakihara, M.; Kadoma, Y.; Kumagai, N.; Mita, H.; Araki, R.; Ozawa, K.; Ozawa, Y. Development of nonflammable lithium ion battery using a new all-solid polymer electrolyte. *J. Solid State Electrochem.* **2012**, *16*, 847–855. [[CrossRef](#)]
47. Youcef, H.B.; Armand, M.; Orayech, B.; Saurel, D.; Shanmukaraj, D. Solid Polymer Electrolyte Based on Modified Cellulose and Its Use in Lithium or Sodium Secondary Batteries. U.S. Patent Application 16/020,568, 3 January 2019.
48. Yushin, G.; Turcheniuk, K.; Yiran, X.; Song, A.-Y.; Borodin, O.; Nitta, N. Solid Electrolyte Technology with Rearrangeable Bonds for Metal and Metal-Ion Batteries. U.S. Patent Application 16/022,572, 3 January 2019.
49. Liu, J.; Liu, Y.; Yang, W.; Ren, Q.; Li, F.; Huang, Z. Lithium ion battery separator with high performance and high safety enabled by tri-layered SiO<sub>2</sub>@PI/m-PE/SiO<sub>2</sub>@PI nanofiber composite membrane. *J. Power Sources* **2018**, *396*, 265–275. [[CrossRef](#)]
50. Herle, S.P.; Gordon, J.G. Ceramic coating on battery separators. U.S. Patent Application 10,193,116, 29 January 2019.
51. Shi, C.; Zhang, P.; Chen, L.; Yang, P.; Zhao, J. Effect of a thin ceramic-coating layer on thermal and electrochemical properties of polyethylene separator for lithium-ion batteries. *J. Power Sources* **2014**, *270*, 547–553. [[CrossRef](#)]
52. Shin, W.-K.; Kim, D.-W. High performance ceramic-coated separators prepared with lithium ion-containing SiO<sub>2</sub> particles for lithium-ion batteries. *J. Power Sources* **2013**, *226*, 54–60. [[CrossRef](#)]

53. Kim, C.-S.; Yoo, J.-S.; Jeong, K.-M.; Kim, K.; Yi, C.-W. Investigation on internal short circuits of lithium polymer batteries with a ceramic-coated separator during nail penetration. *J. Power Sources* **2015**, *289*, 41–49. [[CrossRef](#)]
54. Sun, G.; Dong, G.; Kong, L.; Yan, X.; Tian, G.; Qi, S.; Wu, D. Robust polyimide nanofibrous membrane with porous-layer-coated morphology by in situ self-bonding and micro-crosslinking for lithium-ion battery separator. *Nanoscale* **2018**, *10*, 22439–22447. [[CrossRef](#)] [[PubMed](#)]
55. Orendorff, C.J. The role of separators in lithium-ion cell safety. *Electrochem. Soc. Interface* **2012**, *21*, 61. [[CrossRef](#)]
56. Weber, C.J.; Geiger, S.; Falusi, S.; Roth, M. Material review of Li ion battery separators. *AIP Conf. Proc.* **2014**, 66–81. [[CrossRef](#)]
57. Li, X.; He, J.; Wu, D.; Zhang, M.; Meng, J.; Ni, P. Development of plasma-treated polypropylene nonwoven-based composites for high-performance lithium-ion battery separators. *Electrochim. Acta* **2015**, *167*, 396–403. [[CrossRef](#)]
58. Kong, L.; Wang, Y.; Yu, H.; Liu, B.; Qi, S.; Wu, D.; Zhong, W.H.; Tian, G.; Wang, J. In-Situ Armoring: A Robust, High-Wettability and Fire-Resistant Hybrid Separator for Advanced and Safe Batteries. *ACS Appl. Mater. Interfaces* **2018**. [[CrossRef](#)]
59. Semenov, N.N. *Some Problems in Chemical Kinetics and Reactivity*; Princeton University Press: Princeton, NJ, USA, 1959; Volume 1.
60. Ye, Y.; Saw, L.H.; Shi, Y.; Tay, A.A. Numerical analyses on optimizing a heat pipe thermal management system for lithium-ion batteries during fast charging. *Appl. Therm. Eng.* **2015**, *86*, 281–291. [[CrossRef](#)]
61. Wang, Q.; Sun, Q.; Ping, P.; Zhao, X.; Sun, J.; Lin, Z. Heat transfer in the dynamic cycling of lithium–titanate batteries. *Int. J. Heat Mass Transf.* **2016**, *93*, 896–905. [[CrossRef](#)]
62. Bernardi, D.; Pawlikowski, E.; Newman, J. A general energy balance for battery systems. *J. Electrochem. Soc.* **1985**, *132*, 5. [[CrossRef](#)]
63. Ghiji, M.; Novozhilov, V.; Moinuddin, K.; Joseph, P.; Burch, I.; Suendermann, B.; Gamble, G. A Review of Lithium-Ion Battery Fire Suppression. *Energies* **2020**, *13*, 5117. [[CrossRef](#)]
64. Ouyang, D.; Chen, M.; Huang, Q.; Weng, J.; Wang, Z.; Wang, J. A Review on the Thermal Hazards of the Lithium-Ion Battery and the Corresponding Countermeasures. *Appl. Sci.* **2019**, *9*, 2483. [[CrossRef](#)]
65. Zhong, G.; Mao, B.; Wang, C.; Jiang, L.; Xu, K.; Sun, J.; Wang, Q. Thermal runaway and fire behavior investigation of lithium ion batteries using modified cone calorimeter. *J. Therm. Anal. Calorim.* **2018**. [[CrossRef](#)]
66. Wang, Q.; Huang, P.; Ping, P.; Du, Y.; Li, K.; Sun, J. Combustion behavior of lithium iron phosphate battery induced by external heat radiation. *J. Loss Prev. Process Ind.* **2017**, *49*, 961–969. [[CrossRef](#)]
67. Liu, J.; Wang, Z.; Gong, J.; Liu, K.; Wang, H.; Guo, L. Experimental Study of Thermal Runaway Process of 18650 Lithium-Ion Battery. *Materials* **2017**, *10*, 230. [[CrossRef](#)] [[PubMed](#)]
68. Wang, Z.; Ning, X.; Zhu, K.; Hu, J.; Yang, H.; Wang, J. Evaluating the thermal failure risk of large-format lithium-ion batteries using a cone calorimeter. *J. Fire Sci.* **2019**, *37*, 81–95. [[CrossRef](#)]
69. Ouyang, D.; Chen, M.; Wei, R.; Wang, Z.; Wang, J. A study on the fire behaviors of 18650 battery and batteries pack under discharge. *J. Therm. Anal. Calorim.* **2018**. [[CrossRef](#)]
70. Hatchard, T.D.; Trussler, S.; Dahn, J.R. Building a “smart nail” for penetration tests on Li-ion cells. *J. Power Sources* **2014**, *247*, 821–823. [[CrossRef](#)]
71. Mao, B.; Chen, H.; Cui, Z.; Wu, T.; Wang, Q. Failure mechanism of the lithium ion battery during nail penetration. *Int. J. Heat Mass Transf.* **2018**, *122*, 1103–1115. [[CrossRef](#)]
72. Kitoh, K.; Nemoto, H. 100 Wh Large size Li-ion batteries and safety tests. *J. Power Sources* **1999**, *81–82*, 887–890. [[CrossRef](#)]
73. Zhao, R.; Liu, J.; Gu, J. A comprehensive study on Li-ion battery nail penetrations and the possible solutions. *Energy* **2017**, *123*, 392–401. [[CrossRef](#)]
74. Yokoshima, T.; Mukoyama, D.; Maeda, F.; Osaka, T.; Takazawa, K.; Egusa, S.; Naoi, S.; Ishikura, S.; Yamamoto, K. Direct observation of internal state of thermal runaway in lithium ion battery during nail-penetration test. *J. Power Sources* **2018**, *393*, 67–74. [[CrossRef](#)]
75. Chiu, K.-C.; Lin, C.-H.; Yeh, S.-F.; Lin, Y.-H.; Chen, K.-C. An electrochemical modeling of lithium-ion battery nail penetration. *J. Power Sources* **2014**, *251*, 254–263. [[CrossRef](#)]
76. Liu, B.; Yin, S.; Xu, J. Integrated computation model of lithium-ion battery subject to nail penetration. *Appl. Energy* **2016**, *183*, 278–289. [[CrossRef](#)]
77. Zhao, W.; Luo, G.; Wang, C.-Y. Modeling nail penetration process in large-format Li-ion cells. *J. Electrochem. Soc.* **2014**, *162*, A207. [[CrossRef](#)]
78. Liang, G.; Zhang, Y.; Han, Q.; Liu, Z.; Jiang, Z.; Tian, S. A novel 3D-layered electrochemical-thermal coupled model strategy for the nail-penetration process simulation. *J. Power Sources* **2017**, *342*, 836–845. [[CrossRef](#)]
79. Ichimura, M. The safety characteristics of lithium-ion batteries for mobile phones and the nail penetration test. In Proceedings of the INTELEC 07-29th International Telecommunications Energy Conference, Rome, Italy, 30 September–4 October 2007; pp. 687–692.
80. Liu, X.; Stolarov, S.I.; Denlinger, M.; Masias, A.; Snyder, K. Comprehensive calorimetry of the thermally-induced failure of a lithium ion battery. *J. Power Sources* **2015**, *280*, 516–525. [[CrossRef](#)]
81. Liu, X.; Wu, Z.; Stolarov, S.I.; Denlinger, M.; Masias, A.; Snyder, K. Heat release during thermally-induced failure of a lithium ion battery: Impact of cathode composition. *Fire Saf. J.* **2016**, *85*, 10–22. [[CrossRef](#)]
82. Said, A.O.; Lee, C.; Liu, X.; Wu, Z.; Stolarov, S.I.J.P.o.t.C.I. Simultaneous measurement of multiple thermal hazards associated with a failure of prismatic lithium ion battery. *Proc. Combust. Inst.* **2019**, *37*, 4173–4180.



83. Feng, X.; Fang, M.; He, X.; Ouyang, M.; Lu, L.; Wang, H.; Zhang, M. Thermal runaway features of large format prismatic lithium ion battery using extended volume accelerating rate calorimetry. *J. Power Sources* **2014**, *255*, 294–301. [[CrossRef](#)]
84. Perea, A.; Paoletta, A.; Dubé, J.; Champagne, D.; Mauger, A.; Zaghbi, K. State of charge influence on thermal reactions and abuse tests in commercial lithium-ion cells. *J. Power Sources* **2018**, *399*, 392–397. [[CrossRef](#)]
85. Wang, Z.; Ouyang, D.; Chen, M.; Wang, X.; Zhang, Z.; Wang, J. Fire behavior of lithium-ion battery with different states of charge induced by high incident heat fluxes. *J. Therm. Anal. Calorim.* **2018**. [[CrossRef](#)]
86. Larsson, F.; Andersson, P.; Blomqvist, P.; Lorén, A.; Mellander, B.-E. Characteristics of lithium-ion batteries during fire tests. *J. Power Sources* **2014**, *271*, 414–420. [[CrossRef](#)]
87. Chen, M.; Zhou, D.; Chen, X.; Zhang, W.; Liu, J.; Yuen, R.; Wang, J. Investigation on the thermal hazards of 18650 lithium ion batteries by fire calorimeter. *J. Therm. Anal. Calorim.* **2015**, *122*, 755–763. [[CrossRef](#)]
88. Ping, P.; Wang, Q.; Huang, P.; Li, K.; Sun, J.; Kong, D.; Chen, C. Study of the fire behavior of high-energy lithium-ion batteries with full-scale burning test. *J. Power Sources* **2015**, *285*, 80–89. [[CrossRef](#)]
89. Zheng, Y.; He, Y.-B.; Qian, K.; Li, B.; Wang, X.; Li, J.; Miao, C.; Kang, F. Effects of state of charge on the degradation of LiFePO<sub>4</sub>/graphite batteries during accelerated storage test. *J. Alloys Compd.* **2015**, *639*, 406–414. [[CrossRef](#)]
90. Ouyang, D.; Liu, J.; Chen, M.; Weng, J.; Wang, J. An experimental study on the thermal failure propagation in lithium-ion battery pack. *J. Electrochem. Soc.* **2018**, *165*, A2184.
91. Ouyang, D.; Liu, J.; Chen, M.; Weng, J.; Wang, J. Thermal failure propagation in lithium-ion battery modules with various shapes. *Appl. Sci.* **2018**, *8*, 1263. [[CrossRef](#)]
92. Lopez, C.F.; Jeevarajan, J.A.; Mukherjee, P.P. Experimental analysis of thermal runaway and propagation in lithium-ion battery modules. *J. Electrochem. Soc.* **2015**, *162*, A1905. [[CrossRef](#)]
93. Larsson, F.; Anderson, J.; Andersson, P.; Mellander, B.-E. Thermal modelling of cell-to-cell fire propagation and cascading thermal runaway failure effects for lithium-ion battery cells and modules using fire walls. *J. Electrochem. Soc.* **2016**, *163*, A2854. [[CrossRef](#)]
94. Burch, I.; Ghiji, M.; Gamble, G.; Suendermann, B.; Joseph, P.; Moinuddin, K.; Novozhilov, V. Lithium-ion Battery Fire Suppression in Submarine Battery Compartments. In Proceedings of the PACIFIC 2019, Sydney, Australia, 8–10 October 2019.
95. Feng, X.; He, X.; Ouyang, M.; Lu, L.; Wu, P.; Kulp, C.; Prasser, S. Thermal runaway propagation model for designing a safer battery pack with 25 Ah LiNi<sub>x</sub>Co<sub>y</sub>Mn<sub>z</sub>O<sub>2</sub> large format lithium ion battery. *Appl. Energy* **2015**, *154*, 74–91. [[CrossRef](#)]
96. Wilke, S.; Schweitzer, B.; Khateeb, S.; Al-Hallaj, S. Preventing thermal runaway propagation in lithium ion battery packs using a phase change composite material: An experimental study. *J. Power Sources* **2017**, *340*, 51–59. [[CrossRef](#)]
97. Spinner, N.S.; Field, C.R.; Hammond, M.H.; Williams, B.A.; Myers, K.M.; Lubrano, A.L.; Rose-Pehrsson, S.L.; Tuttle, S.G. Physical and chemical analysis of lithium-ion battery cell-to-cell failure events inside custom fire chamber. *J. Power Sources* **2015**, *279*, 713–721. [[CrossRef](#)]
98. Gao, S.; Feng, X.; Lu, L.; Ouyang, M.; Kamyab, N.; White, R.E.; Coman, P. Thermal runaway propagation assessment of different battery pack designs using the TF5 draft as framework. *J. Electrochem. Soc.* **2019**, *166*, A1653.
99. Lamb, J.; Orendorff, C.J.; Steele, L.A.M.; Spangler, S.W. Failure propagation in multi-cell lithium ion batteries. *J. Power Sources* **2015**, *283*, 517–523. [[CrossRef](#)]
100. Murmann, P.; Mönnighoff, X.; von Aspern, N.; Janssen, P.; Kalinovich, N.; Shevchuk, M.; Kazakova, O.; Röschenhaler, G.-V.; Cekic-Laskovic, I.; Winter, M. Influence of the fluorination degree of organophosphates on flammability and electrochemical performance in lithium ion batteries: Studies on fluorinated compounds deriving from triethyl phosphate. *J. Electrochem. Soc.* **2016**, *163*, A751.
101. Laoutid, F.; Bonnaud, L.; Alexandre, M.; Lopez-Cuesta, J.M.; Dubois, P. New prospects in flame retardant polymer materials: From fundamentals to nanocomposites. *Mater. Sci. Eng. R Rep.* **2009**, *63*, 100–125. [[CrossRef](#)]
102. Xiang, H.F.; Xu, H.Y.; Wang, Z.Z.; Chen, C.H. Dimethyl methylphosphonate (DMMP) as an efficient flame retardant additive for the lithium-ion battery electrolytes. *J. Power Sources* **2007**, *173*, 562–564. [[CrossRef](#)]
103. Hu, J.; Jin, Z.; Zhong, H.; Zhan, H.; Zhou, Y.; Li, Z. A new phosphonamidate as flame retardant additive in electrolytes for lithium ion batteries. *J. Power Sources* **2012**, *197*, 297–300. [[CrossRef](#)]
104. Ding, M.S.; Xu, K.; Jow, T.R. Effects of tris (2, 2, 2-trifluoroethyl) phosphate as a flame-retarding cosolvent on physicochemical properties of electrolytes of LiPF<sub>6</sub> in EC-PC-EMC of 3: 3: 4 weight ratios. *J. Electrochem. Soc.* **2002**, *149*, A1489. [[CrossRef](#)]
105. Zeng, Z.; Jiang, X.; Wu, B.; Xiao, L.; Ai, X.; Yang, H.; Cao, Y. Bis(2,2,2-trifluoroethyl) methylphosphonate: An Novel Flame-retardant Additive for Safe Lithium-ion Battery. *Electrochim. Acta* **2014**, *129*, 300–304. [[CrossRef](#)]
106. Belov, D.G.; Shieh, D.T. A study of tetrabromobisphenol A (TBBA) as a flame retardant additive for Li-ion battery electrolytes. *J. Power Sources* **2014**, *247*, 865–875. [[CrossRef](#)]
107. Wu, B.; Pei, F.; Wu, Y.; Mao, R.; Ai, X.; Yang, H.; Cao, Y. An electrochemically compatible and flame-retardant electrolyte additive for safe lithium ion batteries. *J. Power Sources* **2013**, *227*, 106–110. [[CrossRef](#)]
108. Li, X.; Li, W.; Chen, L.; Lu, Y.; Su, Y.; Bao, L.; Wang, J.; Chen, R.; Chen, S.; Wu, F. Ethoxy (pentafluoro) cyclotriphosphazene (PFPN) as a multi-functional flame retardant electrolyte additive for lithium-ion batteries. *J. Power Sources* **2018**, *378*, 707–716. [[CrossRef](#)]
109. Moreno, M.; Simonetti, E.; Appetecchi, G.; Carewska, M.; Montanino, M.; Kim, G.-T.; Loeffler, N.; Passerini, S. Ionic liquid electrolytes for safer lithium batteries. *J. Electrochem. Soc.* **2016**, *164*, A6026. [[CrossRef](#)]
110. Chawla, N.; Bharti, N.; Singh, S. Recent advances in non-flammable electrolytes for safer lithium-ion batteries. *Batteries* **2019**, *5*, 19. [[CrossRef](#)]



111. Shi, P.; Zheng, H.; Liang, X.; Sun, Y.; Cheng, S.; Chen, C.; Xiang, H. A highly concentrated phosphate-based electrolyte for high-safety rechargeable lithium batteries. *Chem. Commun.* **2018**, *54*, 4453–4456. [[CrossRef](#)]
112. Safa, M.; Chamaani, A.; Chawla, N.; El-Zahab, B. Polymeric Ionic Liquid Gel Electrolyte for Room Temperature Lithium Battery Applications. *Electrochim. Acta* **2016**, *213*, 587–593. [[CrossRef](#)]
113. Guo, Q.; Han, Y.; Wang, H.; Xiong, S.; Sun, W.; Zheng, C.; Xie, K. Flame Retardant and stable  $\text{Li}_{1.5}\text{Al}_{0.5}\text{Ge}_{1.5}(\text{PO}_4)_3$ -supported ionic liquid gel polymer electrolytes for high safety rechargeable solid-state lithium metal batteries. *J. Phys. Chem. C* **2018**, *122*, 10334–10342.
114. Rectenwald, M.F.; Gaffen, J.R.; Rheingold, A.L.; Morgan, A.B.; Protasiewicz, J.D. Phosphoryl-Rich Flame-Retardant Ions (FRIONs): Towards Safer Lithium-Ion Batteries. *Angew. Chem.* **2014**, *126*, 4257–4260. [[CrossRef](#)]
115. Dagger, T.; Meier, V.; Hildebrand, S.; Brüggemann, D.; Winter, M.; Schappacher, F.M. Safety Performance of 5 Ah Lithium Ion Battery Cells Containing the Flame Retardant Electrolyte Additive (Phenoxy) Pentafluorocyclotriphosphazene. *Energy Technol.* **2018**, *6*, 2001–2010. [[CrossRef](#)]
116. Enotiadis, A.; Fernandes, N.J.; Becerra, N.A.; Zammarano, M.; Giannelis, E.P. Nanocomposite electrolytes for lithium batteries with reduced flammability. *Electrochim. Acta* **2018**, *269*, 76–82. [[CrossRef](#)]
117. Wu, H.; Zhuo, D.; Kong, D.; Cui, Y. Improving battery safety by early detection of internal shorting with a bifunctional separator. *Nat. Commun.* **2014**, *5*, 5193. [[CrossRef](#)] [[PubMed](#)]
118. Ryou, M.H.; Lee, D.J.; Lee, J.N.; Lee, Y.M.; Park, J.K.; Choi, J.W. Excellent cycle life of lithium-metal anodes in lithium-ion batteries with mussel-inspired polydopamine-coated separators. *Adv. Energy Mater.* **2012**, *2*, 645–650. [[CrossRef](#)]
119. Kim, J.-H.; Kim, J.-H.; Choi, K.-H.; Yu, H.K.; Kim, J.H.; Lee, J.S.; Lee, S.-Y. Inverse opal-inspired, nanoscaffold battery separators: A new membrane opportunity for high-performance energy storage systems. *Nano Lett.* **2014**, *14*, 4438–4448. [[CrossRef](#)] [[PubMed](#)]
120. Yeon, D.; Lee, Y.; Ryou, M.-H.; Lee, Y.M. New flame-retardant composite separators based on metal hydroxides for lithium-ion batteries. *Electrochim. Acta* **2015**, *157*, 282–289. [[CrossRef](#)]
121. Costa, C.M.; Kundu, M.; Cardoso, V.F.; Machado, A.V.; Silva, M.M.; Lanceros-Méndez, S. Silica/poly(vinylidene fluoride) porous composite membranes for lithium-ion battery separators. *J. Membr. Sci.* **2018**, *564*, 842–851. [[CrossRef](#)]
122. Liu, J.; Yang, K.; Mo, Y.; Wang, S.; Han, D.; Xiao, M.; Meng, Y. Highly safe lithium-ion batteries: High strength separator from polyformaldehyde/cellulose nanofibers blend. *J. Power Sources* **2018**, *400*, 502–510. [[CrossRef](#)]
123. Wang, Q.; Mao, B.; Stolarov, S.I.; Sun, J. A review of lithium ion battery failure mechanisms and fire prevention strategies. *Prog. Energy Combust. Sci.* **2019**, *73*, 95–131. [[CrossRef](#)]
124. Kong, L.; Li, C.; Jiang, J.; Pecht, M.G. Li-ion battery fire hazards and safety strategies. *Energies* **2018**, *11*, 2191. [[CrossRef](#)]
125. Austin Mier, F.; Hargather, M.J.; Ferreira, S.R. Experimental quantification of vent mechanism flow parameters in 18650 format lithium ion batteries. *J. Fluids Eng.* **2019**, *141*, 061403. [[CrossRef](#)]
126. Zhang, H.; Pang, J.; Ai, X.; Cao, Y.; Yang, H.; Lu, S. Poly(3-butylthiophene)-based positive-temperature-coefficient electrodes for safer lithium-ion batteries. *Electrochim. Acta* **2016**, *187*, 173–178. [[CrossRef](#)]
127. Meyer, J. Glass transition temperature as a guide to selection of polymers suitable for PTC materials. *Polymer Eng. Sci.* **1973**, *13*, 462–468. [[CrossRef](#)]
128. Johnson, B.A.; White, R.E. Characterization of commercially available lithium-ion batteries. *J. Power Sources* **1998**, *70*, 48–54. [[CrossRef](#)]
129. Huo, W.; Qu, Y. Effects of  $\text{Bi}_{1/2}\text{Na}_{1/2}\text{TiO}_3$  on the Curie temperature and the PTC effects of  $\text{BaTiO}_3$ -based positive temperature coefficient ceramics. *Sens. Actuators A Phys.* **2006**, *128*, 265–269. [[CrossRef](#)]
130. Ding, S.W.; Jia, G.; Wang, J.; He, Z.Y. Electrical properties of Y- and Mn-doped  $\text{BaTiO}_3$ -based PTC ceramics. *Ceram. Int.* **2008**, *34*, 2007–2010. [[CrossRef](#)]
131. Zhao, S.; Lou, D.; Zhan, P.; Li, G.; Dai, K.; Guo, J.; Zheng, G.; Liu, C.; Shen, C.; Guo, Z. Heating-induced negative temperature coefficient effect in conductive graphene/polymer ternary nanocomposites with a segregated and double-percolated structure. *J. Mater. Chem. C* **2017**, *5*, 8233–8242.
132. Long, R.T.; Blum, A.F.; Bress, T.J.; Cotts, B.R. *Best Practices for Emergency Response to Incidents Involving Electric Vehicles Battery Hazards: A Report on Full-Scale Testing Results*; National Fire Protection Research Foundation: Quincy, MA, USA, 2013; p. 110.
133. Maloney, T. *Extinguishment of Lithium-Ion and Lithium-Metal Battery Fires*; US Federal Aviation Administration: Washington, DC, USA, 2014; pp. 46–51.
134. Hill, D. *Considerations for Energy Storage Systems (ESS) Fire Safety*; OAPUS301WIKO(PP151894), Rev. 4; Det Norske Veritas (U.S.A.), Inc. (DNV GL): Dublin, OH, USA, 9 February 2017.
135. Ribière, P.; Grugeon, S.; Morcrette, M.; Boyanov, S.; Laruelle, S.; Marlair, G. Investigation on the fire-induced hazards of Li-ion battery cells by fire calorimetry. *Energy Environ. Sci.* **2012**, *5*, 5271–5280. [[CrossRef](#)]
136. Fu, Y.; Lu, S.; Shi, L.; Cheng, X.; Zhang, H. Combustion characteristics of electrolyte pool fires for lithium ion batteries. *J. Electrochem. Soc.* **2016**, *163*, A2022. [[CrossRef](#)]
137. Eshetu, G.G.; Grugeon, S.; Laruelle, S.; Boyanov, S.; Lecocq, A.; Bertrand, J.-P.; Marlair, G. In-depth safety-focused analysis of solvents used in electrolytes for large scale lithium ion batteries. *Phys. Chem. Chem. Phys.* **2013**, *15*, 9145–9155. [[CrossRef](#)] [[PubMed](#)]
138. Beyler, C.; Croce, P.; Dubay, C.; Johnson, P.; McNamee, M. Oxygen consumption calorimetry, William Parker: 2016 DiNenno Prize. *Fire Sci. Rev.* **2017**, *6*. [[CrossRef](#)]

139. Huang, P.; Wang, Q.; Li, K.; Ping, P.; Sun, J. The combustion behavior of large scale lithium titanate battery. *Sci. Rep.* **2015**, *5*, 7788. [[CrossRef](#)] [[PubMed](#)]
140. Rao, H.; Huang, Z.; Zhang, H.; Xiao, S. Study of fire tests and fire safety measures on lithium ion battery used on ships. In Proceedings of the 2015 International Conference on Transportation Information and Safety (ICTIS), Wuhan, China, 25–28 June 2015; pp. 865–870.
141. Wang, Q.; Ping, P.; Sun, J. Catastrophe analysis of cylindrical lithium ion battery. *Nonlinear Dyn.* **2010**, *61*, 763–772. [[CrossRef](#)]
142. Hatchard, T.; MacNeil, D.; Basu, A.; Dahn, J.R. Thermal model of cylindrical and prismatic lithium-ion cells. *J. Electrochem. Soc.* **2001**, *148*, A755. [[CrossRef](#)]
143. Kim, G.-H.; Pesaran, A.; Spotnitz, R. A three-dimensional thermal abuse model for lithium-ion cells. *J. Power Sources* **2007**, *170*, 476–489. [[CrossRef](#)]
144. Esho, I.; Shah, K.; Jain, A. Measurements and modeling to determine the critical temperature for preventing thermal runaway in Li-ion cells. *Appl. Therm. Eng.* **2018**, *145*, 287–294. [[CrossRef](#)]
145. Anderson, J.; Larsson, F.; Andersson, P.; Mellander, B.-E. Thermal Modeling of Fire Propagation in Lithium-Ion Batteries. Proceedings of The 24th International Technical Conference on the Enhanced Safety of Vehicles (ESV), Gothenburg, Sweden, 8–11 June 2015.
146. Feng, X.; Lu, L.; Ouyang, M.; Li, J.; He, X. A 3D thermal runaway propagation model for a large format lithium ion battery module. *Energy* **2016**, *115*, 194–208. [[CrossRef](#)]
147. Huang, P.; Ping, P.; Li, K.; Chen, H.; Wang, Q.; Wen, J.; Sun, J. Experimental and modeling analysis of thermal runaway propagation over the large format energy storage battery module with  $\text{Li}_4\text{Ti}_5\text{O}_{12}$  anode. *Appl. Energy* **2016**, *183*, 659–673. [[CrossRef](#)]
148. Huang, P.; Chen, H.; Verma, A.; Wang, Q.; Mukherjee, P.; Sun, J. Non-dimensional analysis of the criticality of Li-ion battery thermal runaway behavior. *J. Hazard. Mater.* **2019**, *369*, 268–278. [[CrossRef](#)]
149. Harris, S.J.; Timmons, A.; Pitz, W.J. A combustion chemistry analysis of carbonate solvents used in Li-ion batteries. *J. Power Sources* **2009**, *193*, 855–858. [[CrossRef](#)]
150. Fernandes, Y.; Bry, A.; de Persis, S. Identification and quantification of gases emitted during abuse tests by overcharge of a commercial Li-ion battery. *J. Power Sources* **2018**, *389*, 106–119. [[CrossRef](#)]
151. Johnsplass, J.; Henriksen, M.; Vaagsaether, K.; Lundberg, J.; Bjerketvedt, D. Simulation of Burning Velocities in Gases Vented from Thermal Run-A-Way Lithium Ion Batteries. In Proceedings of the 58th Conference on Simulation and Modelling (SIMS 58), Reykjavik, Iceland, 25–27 September 2017.